Title: Mechanical damage induced by the appearance of rectified bubble growth in a viscoelastic medium during boiling histotripsy exposure

Author names and affiliations: Ki Joo Pahk[1], Matheus Oliveira de Andrade[2], Pierre Gélat[2], Hyungmin Kim[1] and Nader Saffari[2]

[1]Center for Bionics, Biomedical Research Institute, Korea Institute of Science and Technology (KIST), Seoul, 02792, Republic of Korea

[2]Department of Mechanical Engineering, University College London, London, WC1E 7JE, UK

E-mails:

kjpahk@kist.re.kr (Ki Joo Pahk)

andrade.m@ucl.ac.uk (Matheus Oliveira de Andrade)

p.gelat@ucl.ac.uk (Pierre Gélat)

hk@kist.re.kr (Hyungmin Kim)

n.saffari@ucl.ac.uk (Nader Saffari)

Corresponding authors:

Ki Joo Pahk

Center for Bionics, Biomedical Research Institute, Korea Institute of Science and Technology (KIST), Seoul, 02792, Republic of Korea

E-mail: kjpahk@kist.re.kr

Hyungmin Kim

Center for Bionics, Biomedical Research Institute, Korea Institute of Science and Technology (KIST), Seoul, 02792, Republic of Korea

E-mail: hk@kist.re.kr

Nader Saffari

Department of Mechanical Engineering, University College London, London, WC1E 7JE, UK

E-mail: n.saffari@ucl.ac.uk

Abstract

In boiling histotripsy, the presence of a boiling vapour bubble and understanding of its dynamic behaviour are crucially important for the initiation of the tissue fractionation process and for the control of the size of a lesion produced. Whilst many *in vivo* studies have shown the feasibility of using boiling histotripsy in mechanical fractionation of solid tumours, not much is known about the evolution of a boiling vapour bubble in soft tissue induced by boiling histotripsy. The main objective of this present study is therefore to investigate the formation and dynamic behaviour of a boiling vapour bubble which occurs under boiling histotripsy insonation. Numerical and experimental studies on the bubble dynamics induced in optically transparent tissue-mimicking gel phantoms exposed to the field of a 2.0 MHz High Intensity Focused Ultrasound (HIFU) transducer were performed with a high speed camera. The Gilmore-Zener bubble model coupled with the Khokhlov-Zabolotskaya-Kuznetsov and the Bio-heat Transfer equations was used to simulate bubble dynamics driven by boiling histotripsy waveforms (nonlinear-shocked wave excitation) in a viscoelastic medium as functions of surrounding temperature and of tissue elasticity variations. *In vivo* animal experiments were also conducted to examine cellular structures around a freshly created lesion in the liver resulting from boiling histotripsy. To the best of our knowledge, this is the first study reporting the numerical and experimental evidence of the appearance of rectified bubble growth in a viscoelastic medium. Accounting for tissue phantom elasticity adds a mechanical constraint on vapour bubble growth, which improves the agreement between the simulation and the experimental results. In addition the numerical calculations showed that the asymmetry in a shockwave and water vapour transport can result in rectified bubble growth which could be responsible for HIFU-induced tissue decellularisation. Strain on liver tissue induced by this radial motion can damage liver tissue while preserving blood vessels.

Keywords: high intensity focused ultrasound; boiling histotripsy; acoustic cavitation; rectified bubble growth; tissue decellularisation.

1. Introduction

High Intensity Focused Ultrasound (HIFU) is a promising non-invasive ultrasound technique which has been used to thermally necrose soft tissue [1, 2]. Recent *in vivo* studies on kidney, prostrate, heart and liver have reported that mechanical tissue fractionation with a high degree of precision can also be achieved by HIFU [3–11]. This technique is known as histotripsy and utilises a number of micro or millisecond-long ultrasound pulses with high acoustic peak positive (P_+) and negative (P_-) pressures at the HIFU focus to fractionate soft tissue [12,13]. For histotripsy, peak pressure values of $P_+ > 40$ MPa and P_- of < 10–15 MPa at the focus are typically employed which are comparable to those in the shockwaves used in lithotripsy for kidney stone fragmentation [14, 15].

In general two different methods, known as cavitation cloud histotripsy and boiling histotripsy, are currently being used for inducing mechanical tissue fractionation [16]. The mechanisms of actions involved in these two methods are different; however, both methods can produce a well-defined mechanically fractionated lesion which contains tissue fragments and is sharply demarcated between treated and untreated regions with no sign of thermal damage at the periphery of the lesion [16]. Cavitation cloud histotripsy uses microsecond-long HIFU pulses with driving frequencies of 0.75 MHz to 1.0 MHz and $P_+ > 80$ MPa and P_- = 15–30 MPa at the focus [17, 18]. Because the pressure threshold for cavitation clouds is –28 MPa for most soft tissues [18], peak pressure values used in cavitation cloud histotripsy can lead to the formation of cavitation clouds at the focus, resulting in the mechanical disruption of soft tissue. One to twenty acoustic cycles are generally delivered in a single HIFU pulse with the pulse repetition frequency (PRF) of 10 Hz to 1 kHz and a low duty cycle (less than 1%) to prevent an accumulation of heat at the HIFU focus [17–19]. Though cavitation cloud histotripsy has been shown to be a promising HIFU technique to mechanically fractionate tissue, one of its drawbacks is that the formation of cavitation clouds is a probabilistic event due to the stochastic nature of cavitation activity which depends upon the location and number of pre-existing bubble nuclei within soft tissue [13, 20]. Cavitation activity can, therefore, stop unexpectedly during the course of HIFU exposure [13]. In addition, very large and highly focused HIFU transducers (*f*-number < 0.8) driven by an extremely high radio frequency power amplifier (of the order of several kilowatts) are generally required to achieve high focal peak negative pressures for producing and maintaining the bubble clouds at the focus [8].

An alternative to cavitation cloud histotripsy has been proposed and its efficacy demonstrated [13, 21]. This is known as boiling histotripsy, which uses shock wave heating to produce a boiling vapour bubble and fractionate bulk tissue with a number of millisecond long HIFU pulses. The time taken to form a boiling bubble (i.e., time to boil, t_b) can be predicted theoretically [21]. In boiling histotripsy, peak positive and negative pressures of $P_+ > 40$ MPa and $P_- < 10$–15 MPa are generally produced at the HIFU focus with driving frequencies between 1 MHz and 3 MHz, a PRF of 0.5 – 1 Hz and a duty cycle of ~1%. In contrast to cavitation cloud histotripsy, boiling histotripsy requires significantly less power (of the order of hundreds of watts) and the requirements on the size, focusing gain (*f*-number ~ 1) and frequency of the HIFU source are relatively less restrictive. Therefore, commercially available HIFU systems can be used to perform boiling histotripsy [8, 19, 22]. The shape of a lesion resulting from boiling histotripsy is tadpole like, consisting of a “head” and a “tail” with the “head” closest to the HIFU transducer [23]. The mechanisms of boiling histotripsy are as follows. The production of a shock wavefront at the HIFU focus due to nonlinear wave propagation effects in tissue enables the tissue heating rate to be increased significantly. This localised heating can increase tissue temperature to boiling temperature in a few milliseconds followed by the formation of a boiling bubble at the HIFU focus [21]. After the creation of a boiling bubble, the interaction between incoming shockwaves and the acoustic fields backscattered by the bubble can lead to the generation of an inertial cavitation cluster in front of the boiling bubble towards the HIFU source [24]. The shear forces produced around oscillating boiling bubbles in a localised heated region within the HIFU focal volume may tear off tissue and inertial cavitation clouds enable the mechanical disruption of tissue through violent bubble collapses. These two different types of bubble dynamics, a boiling bubble in the HIFU focus and a cavitation cluster in between the boiling bubble and the HIFU transducer, can result in the production of a “tail” and a “head” of the lesion, respectively [24].

In boiling histotripsy, the presence of a boiling vapour bubble and understanding of its dynamic behaviour are essentially important to initiate the tissue fractionation process as well as to control the size of a lesion produced at a given HIFU exposure condition [24]. Whilst many *in vivo* studies have shown the feasibility of using boiling histotripsy to mechanically break down solid tumours, not much is known about the evolution of a boiling vapour bubble at the HIFU focus in a viscoelastic medium during boiling histotripsy exposure. To that end, the main objective of this study is to investigate the formation and dynamic behaviour of a boiling vapour during boiling histotripsy insonation. Numerical and experimental studies of the bubble dynamics induced in an optically transparent tissue mimicking gel phantom exposed to HIFU fields are performed with a high speed camera and a passive cavitation detection (PCD) system. The Gilmore, the Zener viscoelastic, the Khokhlov-Zabolotskaya-Kuznetsov (KZK) and the Bio-heat Transfer (BHT) equations are used to simulate the dynamics of a single spherical bubble driven by nonlinear-shocked waves in a viscoelastic medium as a function of the surrounding temperature and of elasticity variations.

Furthermore, *in vivo* experiments are conducted to examine cellular structures around a mechanically fractionated lesion resulting from boiling histotripsy exposure.

2. Numerical Bubble Model

The three most used numerical models describing the dynamics of a single spherical bubble exposed to ultrasound fields in a liquid are the Rayleigh-Plesset (RP) [26], Herring-Trilling (HT) [27, 28] and the Gilmore [29] equations. It is extremely important to choose a suitable bubble model to study bubble dynamics since all the models are based on slightly different assumptions.

The Rayleigh-Plesset (RP) equation is one of the simplest models to describe radial bubble motion. This model assumes that the sound velocity is infinite in an incompressible fluid of constant density. The RP equation provides satisfactory numerical results only for small bubble oscillation amplitudes with relatively low flow velocity. Neppiras [30] numerically showed that the RP equation gives validated results for stable cavitation over limited number of acoustic cycles and for inertial cavitation only where the bubble wall velocity is below one fifth of the speed of sound in the liquid. The derivation of the RP model ignores the compressibility of the surrounding liquid and its influence upon bubble dynamics. The effects of the compressibility on radial bubble oscillations, however, become significant for cases in which the bubble wall velocity is comparable with the acoustic velocity in the surrounding medium. Herring [27] and Trilling [28] rederived and modified the RP equation to take into account both the energy stored in the liquid during radial bubble oscillations and the damping effect introduced by the re-radiation of sound fields from bubble oscillations. The HT equation is valid when the bubble wall velocity is small compared to the speed of sound in the liquid. This bubble model is therefore only suitable for small to medium bubble radial oscillations with relatively moderate flow velocity, and violent bubble oscillations (i.e., bubble wall velocity ≥ speed of sound in the surrounding medium) cannot be studied. Gilmore [29] improved the HT model using the Kirkwood-Bethe hypothesis [31] to take into account the compressibility of the liquid and the variation of sound velocity in the liquid as a function of the radial bubble motion. The Kirkwood-Bethe hypothesis [31] states that the sound velocity is equal to the sum of the velocity of the surrounding liquid and the local velocity of sound at the bubble wall. The assumptions behind this model make it suitable for studying the dynamics of a single spherical bubble subjected to high acoustic pressure amplitudes such as those encountered in lithotripter shockwave pulses [32–34]. The Gilmore equation can provide satisfactory results in the region of violent radial oscillations where the bubble wall velocity is comparable to, or even greater than, the speed of sound in the liquid [32]. Because the Gilmore equation is particularly well suited to conditions of high acoustic pressures in which the liquid compressibility plays an important role upon bubble dynamics [32, 33], this bubble model was implemented in the present study to describe the dynamic behaviour of a single spherical bubble excited by a nonlinear-shocked wave.

In the literature of HIFU-induced bubble dynamics in soft tissue, it has been pointed out that both tissue relaxation and elasticity should be taken into account for the modelling of bubble dynamics during HIFU exposure [35, 36]. Since the Zener viscoelastic model effectively describes both tissue relaxation time and tissue elasticity, and is considered to be more accurate in modelling tissue viscoelastic behaviour than the Maxwell and the Kelvin-Voigt models [25], the Zener model was adopted here to describe soft tissue viscoelasticity. A detailed justification of using the Gilmore and the Zener models in modelling a single spherical bubble in soft tissue excited by a shockwave can be found elsewhere [25, 32].

The underlying assumptions of the bubble model developed in the present study are that the single spherical bubble is initially at rest, the bubble remains spherical during its oscillations, there is no bubble fragmentation process after the bubble collapses, the internal pressure and temperature inside the bubble are spatially uniform, there is no bubble coalescence process, the initial bubble radius is much smaller than the wavelength of an acoustic excitation, the bubble is initially filled with air (78% N_2, 21% O_2, 1% Ar) and water vapour (H_2O), the gas in the bubble follows the ideal gas law and there is no gravity acting on the bubble. The effects of shape oscillations of the bubble would likely enhance rectified diffusion. This is because of an enlarged bubble surface area available for a greater net flux of gas into the bubble during expansion. But these are assumed to be negligible in the present study. This is because surface tension tends to preserve the spherical shape of an uncoated microbubble and suppress the development of non-spherical shape modes [80].

The Gilmore bubble model coupled with the Zener viscoelastic model is a nonlinear second order differential equation, and is given by [25]

$$R\ddot{R}\left(1-\frac{\dot{R}}{C}\right)+\frac{3}{2}\dot{R}^2\left(1-\frac{\dot{R}}{3C}\right)=\left(1+\frac{\dot{R}}{C}\right)\left(H-\frac{\tau_{rr}+3q}{\rho_L}\right)+\frac{R}{C}\left[\dot{R}\frac{dH}{dR}\left(1-\frac{\dot{R}}{C}\right)-\frac{\dot{\tau}_{rr}+3\dot{q}}{\rho_L}\right] \quad (1)$$

$$H=\frac{m}{m-1}A^{1/m}\rho_L^{-1}\left[\left(P_w+B\right)^{(m-1)/m}-\left(P_\infty+B\right)^{(m-1)/m}\right] \quad (2)$$

$$C=\sqrt{c_0^2+(m-1)H} \quad (3)$$

$$P_w=P_i-\frac{2\sigma}{R}-\frac{4\mu\dot{R}}{R} \quad (4)$$

$$\dot{\tau}_{rr}=\frac{1}{\lambda_{\mathrm{relax}}}\left[\frac{-4G}{3}\left(1-\frac{R_0^3}{R^3}\right)-\frac{4\mu\dot{R}}{R}\right]-\frac{\tau_{rr}}{\lambda_{\mathrm{relax}}} \quad (5)$$

$$\dot{q}=\frac{1}{3\lambda_{\mathrm{relax}}}\left[\frac{-4G}{3R^3}\left(R^3-R_0^3\right)-\frac{4\mu\dot{R}}{R}\right]-\frac{\dot{R}\tau_{rr}}{R}-\frac{q}{\lambda_{\mathrm{relax}}};\quad q=\int_R^\infty\frac{\tau_{rr}}{r}dr \quad (6)$$

A detailed derivation of the Gilmore-Zener model is well documented in [25]. The dot denotes time derivatives, R_0 is the initial bubble radius, R is the bubble radius, $\dot{R}$ is the velocity of the bubble wall, $\ddot{R}$ is the acceleration of the bubble wall, C is the local speed of sound, c_0 is the infinitesimal speed of sound in the liquid, ρ_L is the equilibrium liquid density, H is the liquid enthalpy, $P_\infty = P_0 + P_a$ is the pressure far from the bubble, P_w is the pressure at the bubble wall, P_0 is the ambient pressure of the surrounding liquid and P_a is the applied acoustic pressure. σ and μ are the surface tension and viscosity of the liquid respectively. $B = A - P_0$ and m are the empirical constants of the modified Tait equation of the state for the liquid [37]. τ_{rr} is the stress for motion in radial direction r, G is the tissue elasticity modulus and λ_{relax} is the tissue relaxation time. The pressure inside the bubble P_i can be described using the van der Waals equation of state with the inclusion of both heat and mass transfer at the bubble wall [38]

$$P_i = \frac{R_{\mathrm{gas}} T_b}{v - b_{\mathrm{v}}} - \frac{a_{\mathrm{v}}}{v^2}\,;\;\; v = \frac{N_{\mathrm{A}} \frac{4}{3}\pi R^3}{N_{\mathrm{tot}}} \quad (7)$$

where R_{gas} is the universal gas constant, T_b is the temperature inside the bubble, v is the mixture molar volume in the bubble, N_{A} is the Avogadro's number and $N_{\mathrm{tot}} = N_{\mathrm{air}} + N_{\mathrm{vap}}$ is the total number of molecules in the bubble. N_{air} and N_{vap} are the number of air and water vapour molecules, respectively. The van der Waals constants a_{v} and b_{v} for the van der Waals forces and the volume occupied by the molecules are determined by [38]

$$a_{\mathrm{v}} = a_{\mathrm{air}}\left(\frac{N_{\mathrm{air}}}{N_{\mathrm{tot}}}\right)^2 + a_{\mathrm{vap}}\left(\frac{N_{\mathrm{vap}}}{N_{\mathrm{tot}}}\right)^2 + 2\sqrt{a_{\mathrm{air}} a_{\mathrm{vap}}}\left(\frac{N_{\mathrm{air}}}{N_{\mathrm{tot}}}\right)\left(\frac{N_{\mathrm{vap}}}{N_{\mathrm{tot}}}\right) \quad (8)$$

$$b_{\mathrm{v}} = b_{\mathrm{air}}\left(\frac{N_{\mathrm{air}}}{N_{\mathrm{tot}}}\right)^2 + b_{\mathrm{vap}}\left(\frac{N_{\mathrm{vap}}}{N_{\mathrm{tot}}}\right)^2 + 2\left\{\left[\frac{1}{2}\left(b_{\mathrm{air}}^{1/3} + b_{\mathrm{vap}}^{1/3}\right)\right]\right\}^{1/3}\left(\frac{N_{\mathrm{air}}}{N_{\mathrm{tot}}}\right)\left(\frac{N_{\mathrm{vap}}}{N_{\mathrm{tot}}}\right) \quad (9)$$

a_{air} and b_{air}, and a_{vap} and b_{vap} are the van der Waals constants of air and water vapour, respectively. The constant values are: a_{air} =1.402 × 10^{-1}, a_{vap} = 5.536 × 10^{-1} (J m^3 mol^{-2}), b_{air} = 3.753 × 10^{-5}, b_{vap} = 3.049 × 10^{-5} (m^3 mol^{-1}).

The Gilmore-Zener bubble model employed in the present study accounted for water vapour transport, non-condensable gas transport and heat transfer at the bubble wall using the same formulas used in [39]. A brief explanation of the main components of the model developed is only presented in the following sections, whereas its detailed description can be found in [39].

2.1. Water vapour, non-condensable gas transports and heat transfer

The rates of change of water vapour (H_2O) and non-condensable gas (air) with respect to time are modelled separately at the bubble wall. To model the evaporation and condensation of vapour, the Hertz-Knudsen equation derived from the classical kinetic theory of gasses is employed, which estimates the change of molar rate of water vapour $\dot{n}_{\mathrm{vap}}$ (mol s^{-1}) at the bubble interface [40]

$$\dot{n}_{\mathrm{vap}} = \dot{n}_{\mathrm{vap}}^{\mathrm{evap}} - \dot{n}_{\mathrm{vap}}^{\mathrm{cond}} = \frac{4\pi R^2}{M_{\mathrm{vap}}} \frac{\alpha_m \bar{c}(T_s)}{4} \left[\rho_{\mathrm{vap}}^{\mathrm{sat}} - \rho_{\mathrm{vap}}(R,t)\right]; \bar{c}(T_s) = \sqrt{\frac{8R_{\mathrm{gas}}T_s}{\pi M_{\mathrm{vap}}}} \quad (10)$$

$$\rho_{\mathrm{vap}}^{\mathrm{sat}} = 322\exp\left(b_1\theta^{2/6} + b_2\theta^{4/6} + b_3\theta^{8/6} + b_4\theta^{18/6} + b_5\theta^{37/6} + b_6\theta^{71/6}\right) \text{with } \theta = 1 - T_0/647.096 \quad (11)$$

$$\rho_{\mathrm{vap}} = \frac{M_{\mathrm{vap}}\left(\frac{N_{\mathrm{vap}}}{N_{\mathrm{tot}}}\right)}{v} \quad (12)$$

$\dot{n}_{\mathrm{vap}}^{\mathrm{evap}}$ and $\dot{n}_{\mathrm{vap}}^{\mathrm{cond}}$ are the molar rates of evaporation and condensation of water vapour and M_{vap} is the molar mass of vapour. α_m is the accommodation coefficient for evaporation or condensation, $\bar{c}$ is the average velocity of molecules, $\rho_{\mathrm{vap}}^{\mathrm{sat}}$ is the saturated density of water vapour and ρ_{vap} is the time-varying density of water vapour. In Eq. (11), the constants are: b_1 = –2.0315024, b_2 = –2.6830294, b_3 = –5.38626492, b_4 = –17.2991605, b_5 = –44.7586581 and b_6 = –63.9201063 [41].

Fick’s law with the boundary layer approximation [42–44] is used to estimate the instantaneous rate of change of non-condensable gas $\dot{n}_{\mathrm{g}}$ (mol s^{-1})

$$\dot{n}_{\mathrm{g,i}} = 4\pi R^2 D_{\mathrm{i}} \frac{c_{\infty,\mathrm{i}} - c_{s,\mathrm{i}}}{L_{\mathrm{g,i}}} \quad (13)$$

$$L_{\mathrm{g,i}} = \min\left(\sqrt{\frac{R D_{\mathrm{i}}}{|\dot{R}|}}, \frac{R}{\pi} \right) \quad (14)$$

$$D_{\mathrm{i}} = \frac{1.4 \times 10^{-8}}{\left[1000\,\mu(T_0)\right]^{1.1} V_{m,\mathrm{i}}^{0.6}} \quad (15)$$

The non-condensable gas diffusion boundary layer is presented at the outer boundary of the bubble wall. In Eqs. (13)–(15), the subscript i denotes different gas species (Nitrogen N_2, Oxygen O_2, Argon Ar), L_{g} is the instantaneous characteristic diffusion length, D_{i} is the empirically determined diffusivity of gas in liquids [45] and $c_s = p_i \left(n_{\mathrm{g}} / n_{\mathrm{tot}}\right) K_{\mathrm{H}}^{-1}$ is the instantaneous concentration of molecules per unit volume (mol m^{-3}) at the bubble wall. $c_\infty = p_0 K_{\mathrm{H}}^{-1}$ is the concentration of dissolved gas far from the bubble, and is used as the initial concentration everywhere in the liquid. Henry’s constant K_{H} (Pa m^3 mol^{-1}) for different gas species i as function of temperature can be obtained by [46]

$$K_{\mathrm{H,i}}(T_0) = \left[\frac{\rho_0}{P_0 M_{\mathrm{i}}} \exp\left(A_h + \frac{B_h}{\tau_h} + C_h \ln \tau_h \right) \right]^{-1} \text{with} \quad \tau_h = \frac{T_0}{100} \quad (16)$$

where, M_{i} is the molar mass for gas species i and $V_{m,\mathrm{i}}$ is the diffusion volume of gas. The alphabetical constants A_h, B_h, C_h, V_m for N_2, O_2 and Ar in Eq. (16) are given in Table 1.

Analogously to Eqs. (13) and (14), the rate of heat transferred to the bubble $\dot{Q}$ and the thermal boundary layer thickness L_{th} can be approximated by [43]

$$\dot{Q} = 4\pi R^2 \lambda_{\mathrm{mix}} \frac{T_0 - T_b}{L_{\mathrm{th}}} \quad (17)$$

$$L_{\mathrm{th}} = \min\left(\sqrt{\frac{RK_{\mathrm{mix}}}{|\dot{R}|}}, \frac{R}{\pi} \right) \quad (18)$$

The thermal boundary layer is presented at the outer boundary of the bubble wall. The thermal conductivity of an air-vapour mixture λ_{mix} (W m^{-1}K^{-1}) depends on temperature and density of the gas and vapour. The temperature dependence of the thermal conductivities of air λ'_{air} and of water vapour λ'_{vap} are assumed to be linear and calculated follows [38]

$$\lambda'_{\mathrm{air}} = \alpha_{\mathrm{air}} T_b + \beta_{\mathrm{air}} \quad (19)$$

$$\lambda'_{\mathrm{vap}} = \alpha_{\mathrm{vap}} T_b + \beta_{\mathrm{vap}} \quad (20)$$

where $\alpha_{\mathrm{air}} = 5.39 \times 10^{-5}$ (W m^{-1} K^{-2}), $\beta_{\mathrm{air}} = 0.0108$ (W m^{-1} K^{-1}) for air and $\alpha_{\mathrm{vap}} = 9.98 \times 10^{-5}$ (W m^{-1} K^{-2}), $\beta_{\mathrm{vap}} = -0.0119$ (W m^{-1} K^{-1}) for water vapour. The temperature dependence of the thermal conductivity of the mixture (air and vapour) λ'_{mix} is then expressed as [50]

$$\lambda'_{\mathrm{mix}} = \left(\frac{n_{\mathrm{vap}}}{n_{\mathrm{tot}}} \sqrt{\lambda'_{\mathrm{vap}}} + \frac{n_{\mathrm{air}}}{n_{\mathrm{tot}}} \sqrt{\lambda'_{\mathrm{air}}} \right)^2 \quad (21)$$

The density dependence of the thermal conductivity of the mixture λ_{mix} is calculated by [51]

$$\lambda_{\mathrm{mix}} = \frac{b_{\mathrm{v}}}{v} \left(\frac{1}{y_a} + 1.2 + 0.755 y_a \right) \lambda'_{\mathrm{mix}} \quad (22)$$

$$y_a = \frac{b_{\mathrm{v}}}{v} + 0.6250 \left(\frac{b_{\mathrm{v}}}{v} \right)^2 + 0.2896 \left(\frac{b_{\mathrm{v}}}{v} \right)^3 + 0.1150 \left(\frac{b_{\mathrm{v}}}{v} \right)^4 \quad (23)$$

The thermal diffusivity K_{mix} (m^2 s^{-1}) of the air-vapour mixture in Eq. (18) can be expressed as [43]

$$K_{\mathrm{mix}} = \frac{\lambda_{\mathrm{mix}}}{c_p} \quad (24)$$

$$c_p = \sum_{1}^{4} \frac{f_{\mathrm{i}} + 2}{2} K_{\mathrm{B}} \frac{N_{\mathrm{i}}}{V} \quad (25)$$

where c_p is the specific heat capacity per unit volume at constant pressure (J m^{-3} K^{-1}), N_i/V is the molecular concentration (m^{-3}) at the bubble wall, $V = 4\pi R^3/3$ is the bubble volume and f_i is the number of translational and rotational degrees of freedom of gas species i. K_B is the Boltzmann constant.

2.2. Temperature change of the bubble

The first law of thermodynamics is employed for calculating the internal energy change inside the bubble [42, 52]

$$\dot{E} = \sum_{\mathrm{i}=1}^{4} (h_\mathrm{i} - u_\mathrm{i})\dot{N}_\mathrm{i} + \dot{Q} - \dot{W} \quad (26)$$

$$h_\mathrm{i} = \frac{f_\mathrm{i} + 2}{2} K_\mathrm{B} T_0 \quad (27)$$

$$u_\mathrm{i} = \left[\frac{f_\mathrm{i}}{2} + \sum_{1}^{n} \frac{\theta_n / T_b}{\exp(\theta_n / T_b) - 1} \right] K_\mathrm{B} T_b \quad (28)$$

where $\dot{E}$ is the rate of total energy change, $(h_\mathrm{i} - u_\mathrm{i})\dot{N}_\mathrm{i}$ is the energy loss due to mass diffusion, $\dot{W} = P_i \dot{V}$ is the work done by the bubble expansion and $\dot{V} = 4\pi R^2 \dot{R}$ is the rate of bubble volume change. h_i is the molecular enthalpy and u_i is the internal energy. θ_n represents the characteristic vibrational temperatures in kelvin units. n is the number of the characteristic vibrational temperatures. The values f_i, θ_n and n for air (N_2, O_2, Ar) and water vapour H_2O are given in Table 2. From Eqs. (17)–(28), the rate of temperature change inside the bubble $\dot{T}_b$ (K s^{-1}) can be obtained algebraically

$$\dot{T}_b = \frac{\dot{E}}{C_{v,\mathrm{mix}}} = \frac{\sum_{\mathrm{i}=1}^{4} (h_\mathrm{i} - u_\mathrm{i})\dot{N}_\mathrm{i}}{C_{v,\mathrm{mix}}} + \frac{\dot{Q}}{C_{v,\mathrm{mix}}} - \frac{\dot{W}}{C_{v,\mathrm{mix}}} \quad (29)$$

$$C_{v,\mathrm{mix}} = K_\mathrm{B} \sum_{\mathrm{i}=1}^{4} \left(\frac{f_\mathrm{i}}{2} + \sum_{1}^{n} \left(\frac{(\theta_n / T_b)^2 \exp(\theta_n / T_b)}{(\exp(\theta_n / T_b) - 1)^2} \right) \right) N_\mathrm{i} \quad (30)$$

where $C_{v,\mathrm{mix}}$ is the heat capacity of the gas mixture (air and vapour) at constant volume (J K^{-1}) [42, 52]. The physical constants for the gas dynamics used in the model are displayed in Table 3. In fact, the gas inside the bubble is heated when the bubble is compressed, and heat is conducted away from the bubble into the surrounding liquid when the surrounding medium is cooler. The temperature at the centre of the bubble is, therefore, higher than that of the bubble surface [76]. For simplicity, in the present study, we assumed that the temperature inside the bubble was spatially uniform. A numerical model describing an internal temperature variation as a function of the distance from the centre of the bubble such as the approach used in [79], could possibly be employed. This is, however, beyond the scope of the present study.

2.3. Initial boundary conditions

The initial boundary conditions (at t = 0) were taken as

$$\begin{gathered} R = R_0; \quad \dot{R} = 0; \quad n_{\mathrm{vap}} = \frac{P_v(T_0)}{K_{\mathrm{B}}T_0}\frac{4\pi}{3}R_0^3; \quad n_{\mathrm{N_2}} = 0.78\frac{P_0}{K_{\mathrm{B}}T_0}\frac{4\pi}{3}R_0^3; \\ n_{\mathrm{O_2}} = 0.21\frac{P_0}{K_{\mathrm{B}}T_0}\frac{4\pi}{3}R_0^3; \quad n_{\mathrm{Ar}} = 0.01\frac{P_0}{K_{\mathrm{B}}T_0}\frac{4\pi}{3}R_0^3; \quad T_b = T_0; \quad \dot{\tau}_{rr} = 0; \quad \dot{q} = 0 \end{gathered} \tag{31}$$

where P_v is the water vapour pressure at a given ambient temperature T_0, and is given by [53]

$$P_v = 610\exp\left[\left(\frac{T_0(\mathrm{K})}{273.16} - 1\right)\left(22.486\frac{273.16}{T_0(\mathrm{K})} + 0.3182\frac{T_0(\mathrm{K})}{273.16} - 2.9558\right)\right] \tag{32}$$

The sets of seven coupled ordinary differential Eqs. (1), (5), (6), (10), (13), (17) and (29) were numerically integrated with ode15s in MATLAB® (MathWorks Inc., R2017a).

2.4. The effects of shear modulus on bubble dynamics

The effects of the variation of the tissue elasticity modulus G (from 0 to 1 MPa) on the radial bubble motion $R(t)$ were computed using the present bubble model with the same parameters as employed by [25]: a sinusoidal wave $A\sin(2\pi ft)$, $A = -1$ MPa, $f = 1.0$ MHz, $P_0 = 101.3$ kPa, $\rho_L = 1060$ kg m^{-3}, $c_0 = 1500$ m s^{-1}, $\lambda_{\text{relax}} = 3$ ns, $\sigma = 0.056$ N m^{-1}, $\mu = 0.015$ kg m^{-1}s^{-1}, $R_0 = 1$ μm and $T_0 = 20^{\circ}$C. Numerical results obtained from the present model show qualitative agreement to [25] within an order of magnitude difference. The calculated radius vs time curve with varying G depicted in Fig. 1a clearly indicates that an increase of tissue elasticity G leads to a significant reduction of the bubble radial oscillation. In addition, the present bubble model enables vapour trapping effects as well as an increase in bubble temperature during bubble collapse [54] to be captured (Figs. 1b and c). When the bubble collapses, the water vapour inside the bubble cannot completely diffuse out since the time scale of the bubble collapse becomes much faster than that of diffusion of water vapour out of the bubble. Thus, water vapour is eventually trapped in the bubble. This can result in an increased heat capacity because of the additional number of water vapour particles limiting both the maximum temperature and pressure in the bubble [75].

2.5. Temperature dependent physical properties of liver

The density, speed of sound, viscosity and the surface tension of the liver as a function of temperature (independent of acoustic pressure fields) were assumed to follow similar trends to those of water (72.8% of adult human liver tissue constitute is water [55]), as it is acknowledged that information regarding this is not readily available [56]. The same equations (33)–(36) used in [39] were employed to initially calculate the temperature dependences of the physical properties of water

$$\rho_{0,\text{water}} = 1000\left[1 - \frac{(T_c - 4)^2}{119000 + 1365T_c - 4T_c^2}\right] \text{ with } T_c = T_0(^{\circ}\text{C}) \quad (33)$$

$$c_{0,\text{water}} = 1402.4 + 5.0384\tau - 5.8117\times10^{-2}\tau^2 + 3.3464\times10^{-4}\tau^3 - 1.4826\times10^{-6}\tau^4 + 3.1659\times10^{-9}\tau^5, \text{ with } \tau = T_0(\text{K}) - 273.16 \quad (34)$$

$$\mu_{0,\text{water}} = \frac{1.779\mu\left(T_0 = 20°\text{C}\right)}{1 + 0.03367T_\text{c} + 2.2099\times10^{-4}T_\text{c}^2} \quad (35)$$

$$\sigma_{0,\text{water}} = 0.2358\ \gamma^{1.256}(1 - 0.625\ \gamma),\ \text{with}\ \gamma = 1 - T_0(\text{K})/647.1 \quad (36)$$

$$\text{Liver}\left(T_0\right) = \text{water}_\text{calculated}\left(T_0\right)\times\text{Ratio} \quad (37)$$

Eqs. (33)–(36) respectively give the variation of water density ρ_0 [57], speed of sound c_0 [58], dynamic viscosity μ_0 [59] and surface tension σ_0 [60] with temperature. To estimate the liver properties, the calculated water properties at a given ambient temperature using Eqs. (33)–(36) were multiplied by the ratio of the liver and water properties measured at 20°C (see Eq. (37)). Table 4 shows the properties of water and of liver at 20°C.

3. Experimental Methods

3.1. High Speed Camera Experiments

The same high speed camera experimental setup and the HIFU exposure protocols used in [24] were employed in this present study to investigate the formation and dynamic behaviour of a boiling vapour bubble induced in an optically transparent liver tissue phantom during boiling histotripsy (Fig. 2). The HIFU experiment was conducted in an acrylic water bath filled with degassed and de-ionised water at 20°C. A 2 MHz single element bowl shaped transducer (Sonic Concepts H106, Bothell, WA, USA) with an aperture size of 64 mm, a geometric focal length of 62.6 mm and lateral and axial full width half maximum pressure dimensions of 1.05 mm and 6.67 mm was used for the boiling histotripsy experiments. This 2 MHz transducer, which was previously characterised using a calibrated 0.2 mm PVDF needle hydrophone (Precision Acoustics Ltd, UK) in water [24], was driven by a waveform generation software (Agilent Waveform Builder, CA, USA), a function generator (Agilent 33220A, CA, USA) and a 55 dB linear power amplifier (ENI 1040L, Rochester, NY, USA). During the experiments, an acoustic absorber (AptFlex F28, Precision Acoustics Ltd, UK) was placed in the water bath to minimise ultrasonic reflections. Furthermore, acoustic emissions emitted at the HIFU focus in the tissue phantom were obtained using a 10 MHz focused PCD transducer (Sonic Concepts Y107, Bothell, WA, USA) connected to a digital oscilloscope (LeCroy HDO 6054, Berkshire, UK) capturing the data at a sampling frequency of 0.5 GHz.

The optically transparent tissue phantom used in the present study with a chemical composition given in Table 5, has similar acoustic and thermal properties to those of liver [13] and has been employed in a number of other boiling histotripsy studies [13, 21, 24]. This gel phantom model is clinically relevant to normal liver tissue with *G* of 4.85 kPa [69]. A detailed recipe for making the liver tissue phantom can be found in [24]. Prior to the HIFU exposure, the liver tissue phantom was clamped in a tissue sample holder, which was then attached to a 3-axis positioning system for alignment with the HIFU focus. During the experiments, the HIFU focus was 5 mm below the surface of the tissue phantom. This phantom penetration distance was chosen according to our previous high speed camera [24] and *in vivo* experiments [9, 10] which show the production of a well-defined lesion in the liver as well as in the gel phantom without rupturing their surfaces.

Bubble dynamics induced at the HIFU focus in the tissue phantom during a single boiling histotripsy pulse was filmed using a high speed camera (FASTCAM-ultima APX, Photron, San Diego, CA, USA) with a 12 X Navitar lens (Navitar, Rocester, NY, USA). This camera was operated at 100,000 frames per second (i.e., 1 frame per 20 acoustic cycles), a shutter speed of 1/100,000 s and a pixel resolution of 128 × 32 (24 μm/pixel). All experiments were backlit with an illuminating system (Solarc ELSV-60, General Electric Company, Farfield, CT, USA) whereby optical images appeared as shadowgraphs where HIFU-induced bubbles in the phantom appeared black and the gel phantom appeared grey colour. A camera processor (FASTCAM-ultima APX, Photron, San Diego, CA, USA) was used to trigger the camera and the function generator at the same time to synchronise the image capturing process with HIFU insonation. All captured optical images were then post-processed with Photron FASTCAM Viewer (Photron, San Diego, CA, USA) in order to examine the change in the size of a boiling bubble over time by counting the pixels representing the bubble. Each measurement was repeated three times.

A single 10 ms-long HIFU pulse with P_+ of 85.4 MPa and P_- of – 15.6 MPa at the HIFU focus in the liver tissue phantom (corresponding electrical power supplied to the 2.0 MHz HIFU transducer P_{elect} was 200 W) was used in the experiments. These *in situ* acoustic peak pressure values were obtained by numerically solving the Khokhlov-Zabolotskaya-Kuznetsov (KZK) non-linear wave equation for a given set of input parameters using the HIFU Simulator v1.2 [62]. With this HIFU exposure condition, the corresponding time to reach the boiling temperature of the tissue phantom t_b was calculated using the Bio-Heat Transfer (BHT) equation [63]. Here, boiling is assumed to be at 100°C for aqueous media since the gel phantom consists of 71% water (Table 5). The following physical properties of the liver tissue phantom at the ambient temperature of 20°C were used in the KZK and the BHT models: the speed of sound of 1544 m s^{-1}, mass density of 1044 kg m^{-3}, absorption coefficient of 15 dB $m^{-1}MHz^{-1}$, coefficient of nonlinearity of 4.0, specific heat capacity per unit volume of 5.3×10^6 J $m^{-3}{}^{\circ}C^{-1}$ and the thermal diffusivity of 1.3×10^{-7} J $m^{-2}s^{-1}$ [13]. From the BHT simulation, the computed t_b was 3.66 ms [24].

The KZK equation used in the present study modelled weak shocks because only the first and the second order terms of the Taylor series expansion of the pressure-density relation were used to describe nonlinearity (i.e., accounting for the effects of quadratic nonlinearity). Therefore, a large error between numerically obtained and actual focal pressure values at the HIFU focus may appear at extreme cases. In such cases, a higher order approximation of nonlinearity is necessary (e.g., cubic nonlinearity term). However, the quadratic approximation used in the present study is still valid, because it has been reported that the effects of the neglected higher order terms (i.e., cubic nonlinearity) in the Taylor series expansion in modelling nonlinear acoustics are insignificant for pressure changes of less than 100 MPa [82]. This is in contrast to the Gilmore bubble model used where a considerable calculation error starts to occur when the pressure in the liquid exceeds 10 GPa [33].

3.2. In vivo experiments

We have previously observed that there two different types of cavitation activity (i.e., a boiling bubble and an inertial cavitation cloud) occurred during the course of boiling histotripsy exposure which contribute to the production of a tadpole-shaped lesion in tissue phantom [24]. This observation led us to suggest that the nature of the damage in cellular structures around a "head" and a "tail" of a lesion must be distinct from each other. In this paper, *in vivo* experiments on male Sprague-Dawley rats (6–8 week old and weighing 200–250g) obtained from the Charles-River Laboratories UK Ltd (Margate, Kent, UK) were performed to investigate a cellular structure around a freshly created boiling histotripsy-induced lesion in the liver. This animal's liver is clinically relevant to normal healthy liver tissue with G of 0.6 kPa [83]. The animals were housed in a temperature controlled room (23^{o}C) with a relative humidity of 50 ± 10% and alternate light/dark conditions. All animal experiments were conducted according to the Home Office guidelines under the UK Animals and Scientific Procedures Act 1986. All experiments were performed under isoflurane general anesthesia.

A schematic diagram of the *in vivo* HIFU experimental set up is shown in Fig. 3. The same 2.0 MHz HIFU source and the electronics used to drive the transducer used in the high speed camera experiments were employed for the *in vivo* experiments. The transducer coupled with a custom built transducer-holder filled with degassed and deionised water was placed on the animal's exteriorised liver and the field coupled through a Myler film (PMX 980, HiFi Industrial Film, Stevenage, UK). The holder was then attached to a 3 axis-positioning system (5430, Sherline Products, Vista, CA, USA). Consistent with the high speed camera experiments, the HIFU focus was 5 mm below the surface of the liver and an adjustable laser pointer aligned with the transducer axis was mounted on the positioning system for guiding the HIFU beam on the liver surface laterally. The same HIFU exposure conditions used in the high speed camera experiments with 1% duty cycle, 1 Hz pulse repetition frequency and 10 HIFU pulses were applied to produce a well-defined mechanically fractionated lesion in the liver. This particular set of the exposure condition was confirmed for the generation of a cavity in the liver *in vivo* reported earlier [9, 10]. With an electrical power of P_{elect} 200 W supplied to the HIFU transducer, the simulated *in situ* peak pressure values were P_+ = 80 MPa and P_- = – 15.6 MPa, and the corresponding t_b was predicted to be 2.05 ms. The physical properties of *in vivo* liver used in the KZK and the BHT simulations are displayed in Table 6.

After the HIFU exposure, animals were sacrificed immediately and the liver tissue containing a boiling histotripsy-induced lesion was removed. Sliced liver was then collected for morphological and histological observations. Paraffin-embedded tissue sections were used for haematoxylin and eosin staining (H&E).

4. Results

4.1. Numerical simulation of a single bubble dynamics in the liver

The present bubble model was used to study the dynamics of a single spherical bubble induced in a viscoelastic medium during boiling histotripsy exposure as a function of temperature T_0 and shear modulus G variations of the medium. The simulated dynamic behaviour of a 1 μm bubble in the liver exposed to a nonlinear shocked-wave (P_+ = 85.4 MPa; P_- = – 15.6 MPa) as a function of temperature at a constant G of 2 kPa is plotted in Fig. 4b. It shows that the time of the bubble growth phase increases as T_0 increases followed by the occurrence of rectified growth at T_0 = 100°C (indicated by the red solid line). Shear modulus of G = 2 kPa was chosen in the computation because this is a typical value for normal healthy liver [66]. In addition, a gradual reduction in the amplitude of the bubble radial motion at T_0 = 100°C with increasing G (0, 2, 5, 8, 10 kPa) is observed in Fig. 4(c). Rectified bubble growth can also be obtained with a sinusoidal wave excitation (P_- = – 15.6 MPa) at T_0 = 100°C (Fig. 5); however, the average bubble growth rate is 1.87 times lower than that under the nonlinear shocked waves (P_+ = 85.4 MPa; P_- = – 15.6 MPa). The peak negative pressure amplitude of the sinusoidal wave used in the calculation was matched to that of the shockwave since the acoustic cavitation threshold is dependent upon the peak negative pressure at a given insonation frequency [67]. In Fig 5, the initial bubble radius of 40 μm was chosen, as this simply demonstrated the effect of the different shapes of the acoustic pressure waveforms (i.e., strongly asymmetric vs symmetric waveforms) on the bubble growth in the absence of any heat or mass transfer after only a few acoustic cycles at T_0 = 100°C and G = 2 kPa. No bubble collapses were observed over 100 acoustic cycles with R_0 = 40 μm in the computation. In fact, the size of the initial bubble radius can affect the numerical results obtained in the present work because of the resonance frequency of a given initial bubble radius f_{res} and the ratio of the f_{res} to the insonation frequency f_0. A smaller bubble, for instance, has a higher f_{res} (i.e., short characteristic timescale) which results in more oscillations in a given period of time and eventually leads the bubble to grow faster and larger compared with a larger bubble with a lower f_{res}. Furthermore, the bubble oscillation is in- or out of phase with an applied ultrasound when $f_{res} > f_0$ and $f_{res} < f_0$, respectively, and the radial bubble motion becomes increasingly large for frequencies (f_{res}) near f_0. With the insonation frequency (2 MHz) used in the present work, a resonant bubble radius is around 1.5 μm [76]. The physical properties of the liver used in the bubble simulation are provided in Table 7.

Additional simulations were conducted to investigate whether this rectified growth of an oscillating boiling bubble induced by boiling histotripsy can mechanically fractionate soft tissue (i.e., liver). A time-varying strain ε at the bubble wall ($r = R$) was estimated as $\varepsilon = -2\left(R^3 - R_0^3\right)/\left(3r^3\right)$ [25], and is plotted in Fig.6. It is interesting to note that corresponding calculated strain produced in the liver is well above the ultimate strain of *ex vivo* liver of 0.54; however, is below that of *ex vivo* femoral artery of 0.69 [68].

4.2. High speed camera and in vivo experimental results

A series of high speed camera images captured during a single 10-ms long HIFU pulse in the liver tissue gel phantom with P_+ of 85.4 MPa and P_- of – 15.6 MPa are shown in Fig. 7. These images were obtained at 100,000 fps with one frame taken every 20 acoustic cycles. Similar to our previous experimental observations [24], a boiling vapour bubble of 141 μm in diameter appears (indicated by the red arrow in Fig. 7i) in a localised heated region in the tissue phantom after 3.47 ms of HIFU exposure with difference of 0.19 ms between the temperature simulation (calculated t_b = 3.66 ms, Fig. 7z-ii, [24]) and the high speed camera experiment. This discrepancy is most likely because the boiling temperature of the gel phantom used was assumed to be at 100^{o}C in the present study. Since the refractive index of the phantom changes with temperature during the course of boiling histotripsy exposure, this localised heated region can be seen as a dark elliptical shape at the HIFU focus (Figs. 7b, d, f and h). The extent of the heated region broadens with time due to the accumulation and diffusion of heat which corresponds well to the simulated temperature contour plots depicted in Figs. 7c, e and g. Localised shockwave heating has been experimentally observed in an optically transparent tissue phantom in previous studies [13, 21, 24]. Alongside the generation of a boiling bubble, an increase in the PCD voltage amplitude as well as a sudden appearance of higher order multiple harmonic components of the fundamental frequency (2 MHz) in the spectrogram is observed in Fig. 8. These significant changes in the PCD voltage versus time plot (Fig. 8a) and the corresponding spectrogram (Fig. 8b) are indications of the production of a boiling bubble during boiling histotripsy [21, 39]. Assuming the speed of sound is constant (1482 m/s), a time delay between the PCD signal and the high speed camera results for the formation of a boiling bubble can simply be calculated using the geometric focal length of the PCD transducer of 6.4 cm (provided by the manufacturer, Sonic Concepts, USA). The time delay is to be 0.043 ms. Since a boiling bubble was optically detected at t = 3.47 ms (Fig. 7i), the appearance of this boiling bubble was expected to be around at t = 3.51 ms in the PCD results. Our PCD experimental observations depicted in Fig. 8, however, showed that the indications of the formation of a boiling bubble occurred at t = 3.44 ms. This discrepancy of 2% (i.e., 0.07 ms) is most probably because of the insufficient temporal and spatial resolution of the optical system used in the present study.

After the formation of a boiling bubble at 3.47 ms, its size gets larger and larger over each acoustic cycle (Fig. 7i–r). Fig. 9 shows the simulated radius vs time curve obtained from the present bubble model, demonstrating a qualitative agreement between the simulation and the experimental results. Calculated strain induced on the tissue phantom by this bubble growth is above the fractional strain of liver reported (Fig. 10). Following the rectified growth event, a cavitation cluster in front of the primary boiling bubble toward the HIFU transducer (indicated by the red arrow in Fig. 7t) and a secondary boiling bubble (indicated by the red arrow in Fig. 7u) within the HIFU focal region are visible at 5.17 ms and 5.21 ms respectively, progressing toward the HIFU transducer until the HIFU insonation ceases at 10 ms. Though the bubble activities beyond the pixel resolution of 128 × 32 (24 μm/pixel) used in the present experimental set up cannot be captured, an overall shape of a tadpole like region occupied by the cavitation clouds and the boiling bubbles for a head and a tail respectively can be observed in the gel phantom at the end of the HIFU exposure (Fig. 7w). High speed camera experimental results showing the formation of a well-defined tadpole-shaped lesion in an optically transparent tissue phantom resulting from boiling histotripsy with a larger pixel resolution of 1028 × 128 (24 μm/pixel) and a lower frame rate of 15,000 fps used are available in our previous study [24].

After the HIFU is turned off, the cavitation clouds and the boiling bubbles shrunk slowly and disappeared with time followed by visualisation of a damaged area in the gel (Fig. 7x to z-i).

Fig. 11 shows a freshly created lesion in the liver *in vivo* resulting from the same boiling histotripsy exposure conditions used in the high speed camera experiments with 1 % duty cycle, 1 Hz PRF and 10 HIFU pulses. A tadpole-like mechanically fractionated lesion filled with blood is observed in Fig. 11a. Upon histological examination, broken hepatocyte plates and pits with ragged boundaries between the treated and untreated regions are noticed around the “head” shaped lesion (Fig. 11c–e), whereas the margins of the “tail” are sharply demarcated with smooth boundaries (Fig. 11f, g).

5. Discussion

5.1. Rectified bubble growth during boiling histotripsy

The Gilmore bubble model coupled with the Zener viscoelastic equation was implemented to study bubble dynamics in soft tissue excited by boiling histotripsy exposure (nonlinear shocked waves with P_+ of 85.4 MPa and P_- of –15.6 MPa) as a function of surrounding temperature T_0 and of shear modulus G variations. The shear modulus was varied to represent the different pathological conditions of the liver: G = 0, 2 (normal healthy liver), 5 (fibrotic liver), 8 and 10 (malignant tumour) kPa [66]. From the numerical simulations, it was observed that the radial bubble growth phase persisted for a longer time period with a larger oscillation amplitude with increasing surrounding temperature T_0 (Fig. 4b). Water vapour is the main component of the bubble content at the end of the growth phase at t = 50 μs (i.e., 99.99 % molar basis, Fig 4d). This overall trend is likely to be due to the increased number of available water vapour molecules in the surrounding medium that can transport into a bubble [39], which increases vapour pressure inside the bubble resulting in an enhanced bubble growth (Figs. 4d, e). This increased amount of water vapour in the bubble is due to rectified heat transfer [77, 78]. In contrast, rectified non-condensable gas diffusion has relatively little effect on the bubble growth during the course of boiling histotripsy [39] as the characteristic timescale of gas diffusion is about five orders of magnitude longer than that of the bubble period (Table 8). Since the peak negative pressure phase has a longer duration than the positive pressure phase in a shockwave, this asymmetry in the acoustic waveform shape can further enhance bubble growth as the bubble undergoes expansion relatively longer than contraction [67]. As a result of the effects of the asymmetry in the acoustic waveform together with water vapour transport, rectified bubble growth can appear in the liver; however, its oscillation amplitude is gradually reduced with an increase in shear modulus (Figs. 4, 5). Since the size of a lesion resulting from boiling histotripsy is likely to be proportional to the size of a boiling bubble at the HIFU focus [24], the lesion size produced in normal healthy liver (G = 2 kPa) would be larger than that in a malignant tumour in the liver (G = 10 kPa) at a given HIFU exposure condition (Fig. 6b). This should be taken into account when designing a boiling histotripsy pulsing protocol for targeting different pathological conditions of the liver.

Rectified growth behaviour was also observed in the high speed camera experiments (Fig. 7). Simulated bubble radius vs time curve obtained from the present bubble model plotted in Fig. 9 shows a qualitative agreement with the experimental measurements between t = 3.47 ms and 3.54 ms. There is, however, a discrepancy in bubble radius after t = 3.54 ms where the bubble growth rate accelerated as the bubble grew in the simulation, whereas the experimentally measured size of the bubble did not change significantly after t = 3.54 ms (Figs. 7p–w and 9). This is most probably because of the acoustic shielding effects caused by the production of a cavitation cluster in front of the primary boiling bubble towards the HIFU source [24], which could possibly lead to the reduction of the pressure magnitude as well as the deformation of the acoustic waveform at the focus.

5.2. Mechanical damage induced by bubble dynamics during boiling histotripsy

The overall shape of a mechanically fractionated lesion by boiling histotripsy is tadpole like consisting of a “head” and a “tail” with the head facing towards the HIFU transducer [23]. In [24], with the help of the high speed camera observations of the lesion formation in an optically transparent tissue phantom, we proposed that shear forces on tissue resulting from a rapid boiling bubble expansion produce a "tail" shaped lesion, whereas emissions of micro jetting and shockwaves resulting from an inertial cavitation cluster induce the "head" shaped lesion. To support this hypothesis, one would expect there to be a difference in the nature of the damage in cellular structures between a "tail" and a "head". Based on histological examination of a freshly created cavity (Fig. 11b–g), a number of broken hepatocytes plates and remnants of the interlobular septa (matrix) with some pits were observed around a "head" region. A similar form of cellular damage was observed in a number of cavitation cloud histotripsy studies [17, 70]. Furthermore, the presence of pits is generally the result of inertial cavitation [71]. Contrary to the histologic observations of a "head" lesion, the margins of a "tail" shaped lesion were sharply demarcated between the treated and untreated regions with the absence of broken hepatic plates (Fig. 11f, g). Along with the experimental evidences of inertial cavitation-induced and of shear forces-induced cell damage for a head and a tail respectively, our numerical results reveal that shear forces produced by the dynamics of a vapour bubble during boiling histotripsy can cause selective cellular damage. Calculated time-varying strain on liver tissue plotted in Figs. 6, 10 depicted that strain induced by rectified bubble growth is well above the ultimate fractional strain of liver, but interestingly, is below that of femoral artery (*ex vivo* porcine). This result is of paramount importance for cell therapy (e.g., cell transplantation) suggesting that HIFU-induced liver tissue decellularisation where hepatocytes are selectively destroyed while an extracellular matrix (ECM) scaffold and blood vessels are intact [10] may be achieved by this rectification growth driven by boiling histotripsy. An ECM scaffold with intact blood vessels in a decellularised lesion may enhance cell integration due to the fact that (a) three-dimensional support with an appropriate biological microenvironment promotes cell attachment and proliferation, and (b) cells cannot survive more than a distance of 200 μm away from a blood vessel [16, 72–74].

Production of a boiling histotripsy-induced decellularised lesion in soft tissue with a desired degree of intact ECM through precisely controlling rectified bubble growth phase would, therefore, be of much interest for cell therapy. For this to be achieved, an accurate and reliable numerical bubble model accounting for bubble-bubble interactions or bubble oscillations near cell walls would be required. These could be potentially modelled using boundary element methods such as the approach developed in [81].

6. Conclusions

In this study, a numerical and experimental study of bubble dynamics in a viscoelastic medium induced by boiling histotripsy was performed with a high speed camera and a passive cavitation detection system. To the best of our knowledge, this is the first study reporting the numerical and experimental evidence of the appearance of rectified bubble growth which could be responsible for the production of a HIFU-induced decellularised lesion. Numerical results presented in this study suggest that the asymmetry in a shockwave together with water vapour transport can result in rectified bubble growth that can potentially tear off liver tissue while preserving blood vessels. Further investigations of the prediction of the size of a boiling vapour bubble and the precise control of its dynamics during boiling histotripsy are necessary in the future.

Acknowledgments

This work was supported and funded by the Korea Institute of Science and Technology (KIST, Korea, 2E27980 & 2E27975), the Department of Mechanical Engineering, University College London (UCL, UK) and the Brazilian National Council for Scientific and Technological Development (CNPq).

References

[1] G. ter Haar, C. Coussios, High intensity focused ultrasound: physical principles and devices, Int. J. Hyperthermia 23 (2007) 89–104.

[2] J.F. Aubry, K.B. Pauly, C. Moonen, G. ter Haar, M. Ries, R. Salomir, S. Sokka, K.M. Sekins, Y. Shapira, F. Ye, H. Huff-Simonin, M. Eames, A. Hananel, N. Kassell, A. Napoli, J.H. Hwang, F. Wu, L. Zhang, A. Melzer, Y.S. Kim, W.M. Gedroyc, The road to clinical use of high-intensity focused ultrasound for liver cancer: technical and clinical consensus, J. Ther. Ultrasound 1 (2013) 1–7.

[3] W.W. Roberts, T.L. Hall, K. Ives, J.S. Wolf, J.B. Fowlkes, C.A. Cain, Pulsed cavitational ultrasound: a noninvasive technology for controlled tissue ablation (histotripsy) in the rabbit kidney, J. Urol. 175 (2006) 734–738.

[4] T.L. Hall, C.R. Hempel, K. Wojno, Z. Xu, C.A. Cain, W.W. Roberts, Histotripsy of the prostate: dose effects in a chronic canine model, Urology 74 (2009) 932–937.

[5] N.R. Styn, J.C. Wheat, T.L. Hall, W.W. Roberts, Histotripsy of vx-2 tumor implanted in a renal rabbit model, J. Endourol. 24 (2010) 1145–1150.

[6] Z. Xu, G. Owens, D. Gordon, C. Cain, A. Ludomirsky, Noninvasive creation of an atrial septal defect by histotripsy in a canine model, Circulation 121 (2010) 742–749.

[7] E. Vlaisavljevich, Y. Kim, S. Allen, G. Owens, S. Pelletier, C. Cain, K. Ives, Z. Xu, Image-guided non-invasive ultrasound liver ablation using histotripsy: feasibility study in an in vivo porcine model, Ultrasound Med. Biol. 39 (2013) 1398–1409.

[8] T.D. Khokhlova, Y.N. Wang, J.C. Simon, B.W. Cunitz, F. Starr, M. Paun, L.A. Crum, M.R. Bailey, V.A. Khokhlova, Ultrasound-guided tissue fractionation by high intensity focused ultrasound in an in vivo porcine liver model, Proc. Natl. Acad. Sci. USA 111 (2014) 8161–8166.

[9] K.J. Pahk, D.K. Dhar, M. Malago, N. Saffari, Ultrasonic histotripsy for tissue therapy, J. Phys. Conf. Ser. 581 (2015) 012001.

[10] K.J. Pahk, G.H. Mohammad, M. Malago, N. Saffari, D.K. Dhar, A novel approach to ultrasound-mediated tissue decellularization and intra-hepatic cell delivery in rats, Ultrasound in Med. Biol. 42 (2016) 1958–1967.

[11] M. Hoogenboom, D.C. Eikelenboom, R.J.E. van den Bijgaart, A. Heerschap, P. Wesseling, M.H. den Brok, J.J. Fütterer, G.J. Adema, Impact of MR-guided boiling histotripsy in distinct murine tumor models, Ultrason. Sonochem. 38 (2017) 1–8.

[12] K. Kieran, T.L. Hall, J.E. Parsons, J.S. Wolf, J.B. Fowlkes, C.A. Cain, W.W. Roberts, Refining histotripsy: defining the parameter space for the creation of nonthermal lesions with high intensity, pulsed focused ultrasound of the in vitro kidney, J. Urol. 178 (2007) 672–676.

[13] T.D. Khokhlova, M.S. Canney, V.A. Khokhlova, O.A. Sapozhnikov, L.A. Crum, M.R. Bailey, Controlled tissue emulsification produced by high intensity focused ultrasound shock waves and millisecond boiling, J. Acoust. Soc. Am. 130 (2011) 3498 – 3510.

[14] S. Zhu, F.H. Cocks, G.M. Preminger, P. Zhong P, The role of stress waves and cavitation in stone comminution in shock wave lithotripsy, Ultrasound Med. Biol. 28 (2002) 661–671.

[15] Y.A. Pishchalnikov, O.A. Sapozhnikov, M.R. Bailey, J.C. Williams, R.O. Cleveland, T. Colonius, L.A. Crum, A.P. Evan, J.A. McAteer, Cavitation bubble cluster activity in the breakage of kidney stones by lithotripter shockwaves, J. Endourol. 17 (2003) 435–446.

[16] V.A. Khokhlova, J.B. Fowlkes, W.W. Roberts, G.R. Schade, Z. Xu, T.D. Khokhlova, T.L. Hall, A.D. Maxwell, Y.N. Wang, C.A Cain, Histotripsy methods in mechanical disintegration of tissue: towards clinical applications, Int. J. Hyperthermia 31 (2015) 145–162.

[17] J.E. Parsons, C.A. Cain, G.D. Abrams, J.B. Fowlkes, Pulsed cavitational ultrasound therapy for controlled tissue homogenization, Ultrasound Med. Biol. 32 (2006) 115–129.

[18] K.W. Lin, Y. Kim, A. Maxwell, T.Y. Wang, T.L. Hall, Z. Xu, J.B. Fowlkes, C.A. Cain, Histotripsy beyond the intrinsic cavitation threshold using very short ultrasound pulses: microtripsy, IEEE Trans. Ultrason. Ferroelectr. Freq. Control 61 (2014) 251–265.

[19] A. Maxwell, O. Sapozhnikov, M. Bailey, L. Crum, Z. Xu, B. Fowlkes, C. Cain, V. Khokhlova, Disintegration of tissue using high intensity focused ultrasound: two approaches that utilize shock waves, Acoustics Today 8 (2012) 24–37.

[20] A.D. Maxwell, T.Y. Wang, C.A. Cain, J.B. Fowlkes, O.A. Sapozhnikov, M.R. Bailey, Z. Xu, Cavitation clouds created by shock scattering from bubbles during histotripsy, J. Acoust. Soc. Am. 130 (2011) 1888–1898.

[21] M.S. Canney, V.A. Khokhlova, O.V. Bessonova, M.R. Bailey, L.A. Crum, Shock-induced heating and millisecond boiling in gels and tissue due to high intensity focused ultrasound. Ultrasound Med. Biol. 36 (2010) 250–267.

[22] W. Kreider, P.V. Yuldashev, O.A. Sapozhnikov, N. Farr, A. Partanen, M.R. Bailey, V.A. Khokhlova, Characterization of a multi-element clinical HIFU system using acoustic holography and nonlinear modelling, IEEE Trans. Ultrason. Ferr. Freq. Control. 60 (2013) 1683–1698.

[23] T.D. Khokhlova, J.H. Hwang, HIFU for palliative treatment of pancreatic cancer, J. Gastrointest. Oncol. (2) 2011 175–184.

[24] K.J. Pahk, P. Gélat, D. Sinden, D.K. Dhar, N. Saffari, Numerical and experimental study of mechanisms involved in boiling histotripsy, Ultrasound Med. Biol. 43 (2017) 2848–2861.

[25] E. Zilonova, M. Solovchuk, T.W.H. Sheu, Bubble dynamics in viscoelastic soft tissue in high-intensity focal ultrasound thermal therapy, Ultrason. Sonochem. 40(2018) 900 – 911.

[26] M.S. Plesset, The dynamics of cavitation bubbles. ASME Journal of Applied Mechanics, 16 (1949) 228 – 231.

[27] C. Herring, Theory of the pulsations of the gas bubble produced by an underwater explosion, Columbia Univ, Division of National Defense Research, 1941.

[28] L. Trilling, The collapse and rebound of a gas bubble, J. Appl. Phys. 23 (1952) 14–17.

[29] F.R. Gilmore, The growth or collapse of a spherical bubble in a viscous compressible liquid (1952).

[30] E.A. Neppiras, Acoustic Cavitation. Phys. Rep. 61 (1980) 159–251.

[31] J.G. Kirkwood, H.A. Bethe, H.A, The pressure wave produced by an underwater explosion, Division of National Defense Research, (1942).

[32] K. Vokurka, Comparison of Rayleigh's, Herring's, and Gilmore's models of gas bubbles. Acta. Acust. United Ac. 59 (1986) 214–219.

[33] C.C. Church, A theoretical study of cavitation generated by an extracorporeal shock wave lithotripter. J. Acoust. Soc. Am. 86 (1989) 215–227.

[34] A.D. Phelps, T.G. Leighton, The subharmonic oscillations and combination-frequency subharmonic emissions from a resonant bubble: their properties and generation mechanisms. Acta. Acust. United Ac. 83 (1997) 59–66.

[35] Y. Zheng, X. Chen, A. Yao, H. Lin, Y. Shen, Y. Zhu, M. Lu, T. Wang, S. Chen, Shear wave propagation in soft tissue and ultrasound vibrometry, Wave ropagation Theories and Applications, InTech, 2013.

[36] V. Suomi, Y. Han, E. Konofagou, R.O. Cleveland, The effect of temperature dependent tissue parameters on acoustic radiation force induced displacements, Phys. Med. Biol. 61 (2016) 7427–7447.

[37] F. Chavrier, J.Y. Chapelon, A. Gelet, D. Cathignol, Modeling of high-intensity focused ultrasound-induced lesions in the presence of cavitation bubbles, J. Acoust. Soc. Am. 108 (2000) 432–440.

[38] K. Yasui, Effects of thermal conduction on bubble dynamics near the sonoluminescence threshold, J. Acoust. Soc. Am. 98 (1995) 2772–2782.

[39] K.J. Pahk, P. Gélat, H. Kim, N. Saffari, Bubble dynamics in boiling histotripsy, Ultrasound Med. Biol. 44 (2018) 2673–2696.

[40] J. Holzfuss, Unstable diffusion and chemical dissociation of a single sonoluminescing bubble, Phys. Rev. E., 71 (2005) 1–5.

[41] W. Wagner, A. Pruß, The IAPWS formulation 1995 for the thermodynamic properties of ordinary water substance for general and scientific use, J. Phys. Chem. Ref. Data., 31 (2002) 387–535.

[42] R. Toegel, B. Gompf, R. Pecha, D. Lohse, Does water vapor prevent upscaling sonoluminescence? Phys. Rev. Lett. 85 (2000) 3165–3168.

[43] R. Toegel, D. Lohse, Phase diagrams for sonoluminescing bubbles: a comparison between experiment and theory, J. Chem. Phys. 118(2003) 1863–1875.

[44] L. Stricker, A. Prosperetti, D. Lohse, Validation of an approximate model for the thermal behavior in acoustically driven bubbles, J. Acoust. Soc. Am. 130 (2011) 3243–3251.

[45] D.F. Othmer, M.S. Thakar, Correlating diffusion coefficients in liquids, Ind. Eng. Chem. 45 (1953) 589–593.

[46] R. Battino, T.R. Rettich, T. Tominaga, The solubility of nitrogen and air in liquids, J. Phys. Chem. Ref. Data. 13 (1984) 563–600.

[47] R. Battino, IUPAC Solubility Data Series, Vol. 10 (1982), Nitrogen and Air. Oxford: Pergamon.

[48] R. Battino, IUPAC Solubility Data Series, Vol. 7 (1981), Oxygen and Ozone. Oxford: Pergamon

[49] H.L. Clever, IUPAC Solubility Data Series: Vol. 4 (1980), Argon. Oxford: Pergamon Press.

[50] B.E. Poling, J.M. Prausnitz, J.P. O'Connell, The properties of gases and liquids, 2004 New York: McGraw-Hill.

[51] J.O. Hirschfelder, C.F. Curtiss, R.B. Bird, Molecular Theory of Gases and Liquids, 1964 New York: Wiley.

[52] E. Samiei, M. Shams, R. Ebrahimi, A novel numerical scheme for the investigation of surface tension effects on growth and collapse stages of cavitation bubbles, Eur. J. Mech. B-Fluids, 30 (2011) 41–50.

[53] I.R. Webb, S.J. Payne, C.C. Coussios, The effect of temperature and viscoelasticity on cavitation dynamics during ultrasonic ablation, J. Acoust. Soc. Am., 130 (2011) 3458–3466.

[54] B.D. Storey, A.J. Szeri A J, Water vapour, sonoluminescence and sonochemistry, Proc. R. Soc. London. A. 456 (2000) 1685–1709.

[55] F.A. Duck, Physical properties of tissue: a comprehensive reference book, 1990 London: Academic Press.

[56] M.J. Choi, S.R. Guntur, J.M. Lee, D.G. Paeng, K.I. Lee, A. Coleman, Changes in ultrasonic properties of liver tissue in vitro during heating-cooling cycle concomitant with thermal coagulation, Ultrasound in Med. Biol. 37 **(**2011) 2000–2012.

[57] V.S. Kravchenko, Empirical equation derived for temperature dependence of density of heavy water, Soviet Atomic Energy. 20 (1966) 212.

[58] N. Bilaniuk, G.S.K. Wong, Speed of sound in pure water as a function of temperature, J. Acoust. Soc. Am. 93 (1993) 1609–1612.

[59] D.D. Joseph, Variable viscosity effects on the flow and stability of flow in channels and pipes, Phys. Fluids. **7 (**1964) 1761–1771.

[60] I.R. Webb, S.J. Payne, C.C Coussios, The effect of temperature and viscoelasticity on cavitation dynamics during ultrasonic ablation, J. Acoust. Soc. Am. 130 (2011) 3458–3466.

[61] C.C. Church, C. Labuda, K. Nightingale, Should the mechanical index be revised for ARFI imaging? IEEE Int. Ultras. Symp. Proc., 7-10 October 2012, Dresden, Germany **5 (**2012) 17–20.

[62] J.E. Soneson, A user-friendly software package for HIFU simulation, In: Proceedings of the 8th International Symposium for Therapeutic Ultrasound (2009) 165–169.

[63] H.H. Pennes, Analysis of tissue and arterial blood temperatures in the resting human forearm, J. Appl. Physiol. 1 (1948) 93–122.

[64] M.J. Choi, S.R. Guntur, K.I. Lee, D.G. Paeng, A. Coleman, A tissue mimicking polyacrylamide hydrogel phantom for visualizing thermal lesions generated by high intensity focused ultrasound, Ultrasound in Med. Biol. 39 (2013), 439–448.

[65] E.J. Rijkhorst, I. Rivens, G. ter Haar, D. Hawkes, D. Barratt, Effects of respiratory liver motion on heating for gated and model-based motion-compensated high-intensity focused ultrasound ablation. Proc. 14th Int. Conf. Medical Image Computing and Computer-Assisted Intervention (MICCAI), 18-22 September 2011, Toronto, Canada. 605–612.

[66] S. K. Venkatesh, M. Yin, J.F. Glockner, N. Takahashi, P.A. Araoz, J.A. Talwalkar, R. L. Ehman, Magnetic resonance elastography of liver tumors: preliminary results, AJR Am. J. Roentgenol 190 (2008) 1534–1540.

[67] W. Kreider, M.R. Bailey, O.A. Sapozhnikov, V.A. Khokhlova, L.A. Crum, L.A, The dynamics of histotripsy bubbles, AIP Conf. Proc. 10th Int. Symp. on Therapeutic Ultrasound (ISTU 2010), 9-12 June 2010, Tokyo, Japan. 1359 (2011), 427–430.

[68] E. Vlaisavljevich, Y. Kim, G. Owens, W. Roberts, C. Cain, Z. Xu, Effects of tissue mechanical properties on susceptibility to histotripsy-induced tissue damage, Phys. Med. Biol. 59 (2013) 253–270.

[69] S.R. Guntur, M.J. Choi, An improved tissue-mimicking polyacrylamide hydrogel phantom for visualizing thermal lesions with high-intensity focused ultrasound, Ultrasound in Med. Biol. 40 (2014) 2680–2691.

[70] A.P. Duryea, C.A. Cain, W.W. Roberts, T.L. Hall, Removal of residual cavitation nuclei to enhance histotripsy fractionation of soft tissue, IEEE Trans. Ultrason. Ferroelectr. Freq. Control, 62 (2015), 2068–2078.

[71] A. Tezel, S. Mitragotri, Interactions of inertial cavitation bubbles with stratum corneum lipid bilayers during low-frequency sonophoresis, Biophysical Journal. 85 (2003), 3502–3512.

[72] B. Frerich, N. Lindemann, J. Kurtz-Hoffmann, K. Oertel, In vitro model of a vascular stroma for the engineering of vascularized tissues, Int. J. Oral Maxillofacial Surg., 30 (2001), 414 – 420.

[73] S.F. Badylak, Xenogeneic extracellular matrix as a scaffold for tissue reconstruction, Transpl. Immunol., 12(2004), 367 – 377.

[74] M. Lovett, K. Lee, A. Edwards, D.L. Kaplan, Vascularization strategies for tissue engineering, Tissue Eng. Part B Rev., 15 (2009), 353–370.

[75] M.P. Brenner, S. Hilgenfeldt, D. Lohse, Single-bubble sonoluminescence, Rev. Mod. Phys. 74 (2002), 425 – 484.

[76] H. Feng, G. Barbosa-Canovas, J.Weiss, Ultrasound technologies for food and bioprocessing (2010), New York, Springer.

[77] Y. Hao, A. Prosperetti, The dynamics of vapour bubbles in acoustic pressure fields. Phys. Fluids, 11 (1999), 2008 – 2019.

[78] Y. Hao, A. Prosperetti, Rectified heat transfer into translating pulsating vapor bubbles. J. Acoust Soc. Am., 112 (2002), 1787 – 1797.

[79] A. Prosperetti, The thermal behaviour of oscillating gas bubbles. J. Fluid Mech., 222 (1991), 587 – 616.

[80] Y. Liu, K. Sugiyama, S. Takagi, Y. Matsumoto, Numerical study on the shape oscillation of an encapsulated microbubble in ultrasound field. Phys. Fluids, 23 (2011), 041904.

[81] N Méndez, R. González-Cinca, Numerical study of bubble dynamics with the boundary element method. J. Phys. Conf. Ser., 327 (2011), 012028.

[82] M. S. Canney, M. R. Bailey, L. A Crum. Acoustic characterization of high intensity focused ultrasound fields: a combined measurement and modelling approach. J. Acoust. Soc. Am., 124 (2008), 2046 – 2420.

[83] Zhu Y, Zheng Y, Shen Y, Chen X, Zhang X, Lin H, Guo Y, Wang T, Chen S, Analyzing and modelling rheological behavior of liver fibrosis in rats using shear viscoelastic moduli. J. Zhejiang Univ. Sci. B. 15(2014), 375 – 381.

Figures

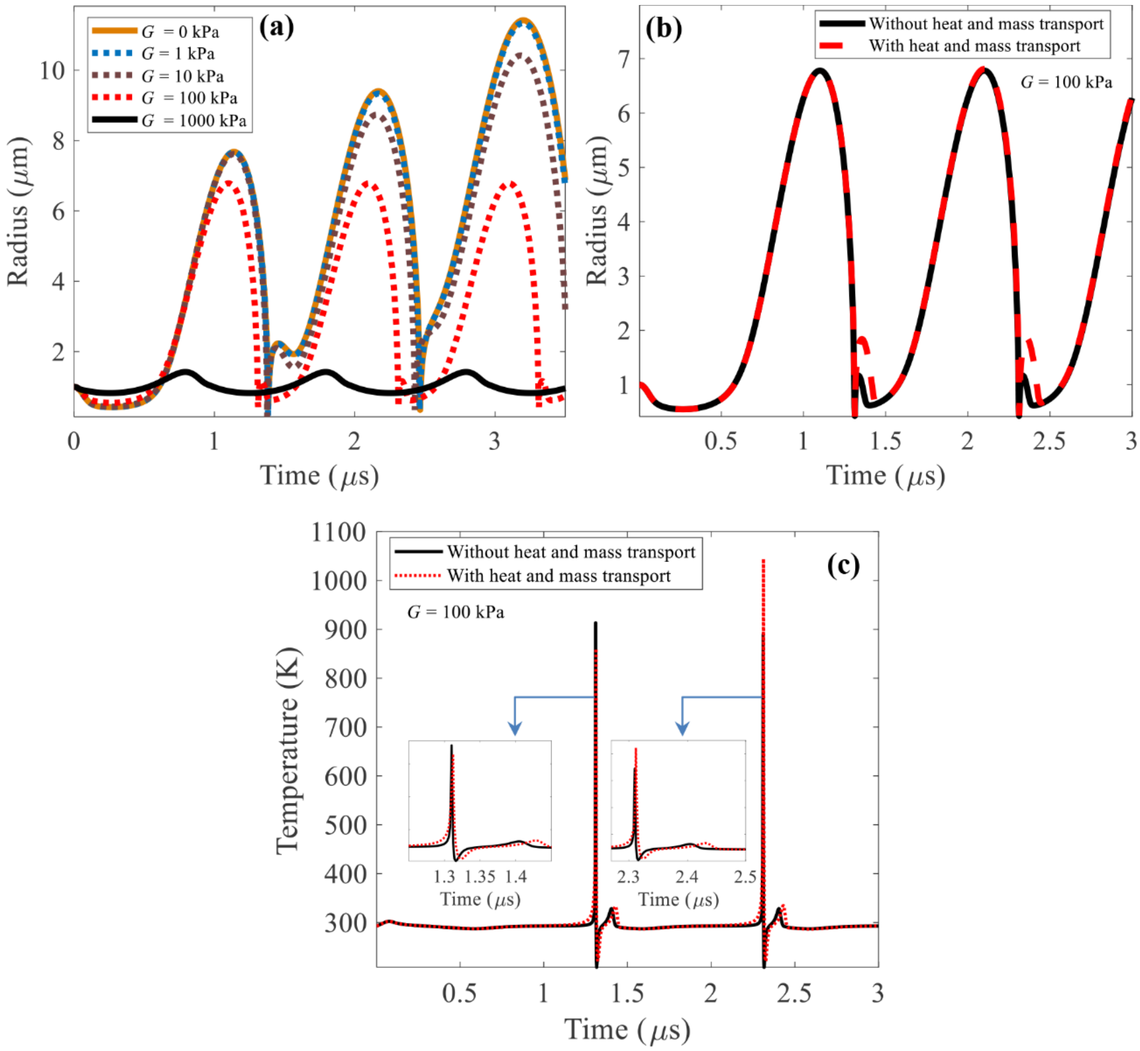

Fig. 1. Simulated bubble dynamics for validation purpose. (a) Radius vs time $R(t)$ curve with varying tissue elasticity modulus G (0, 1, 10, 100 and 1000 kPa). (b) $R(t)$ curve with (indicated by the red dashed lines) and without (indicated by the black solid lines) heat and mass transport at G = 100 kPa. (c) Corresponding bubble temperature profile of (b). The same parameters as employed by [25]: a sinusoidal wave $A\sin(2\pi ft)$, A = -1 MPa, f = 1.0 MHz, P_0 = 101.3 kPa, ρ_L = 1060 kg m^{-3}, c_0 = 1500 m s^{-1}, λ_{relax} = 3 ns, σ = 0.056 N m^{-1}, μ = 0.015 kg m^{-1}s^{-1}, R_0 = 1 μm and T_0 = 20°C, were used in the present calculation.

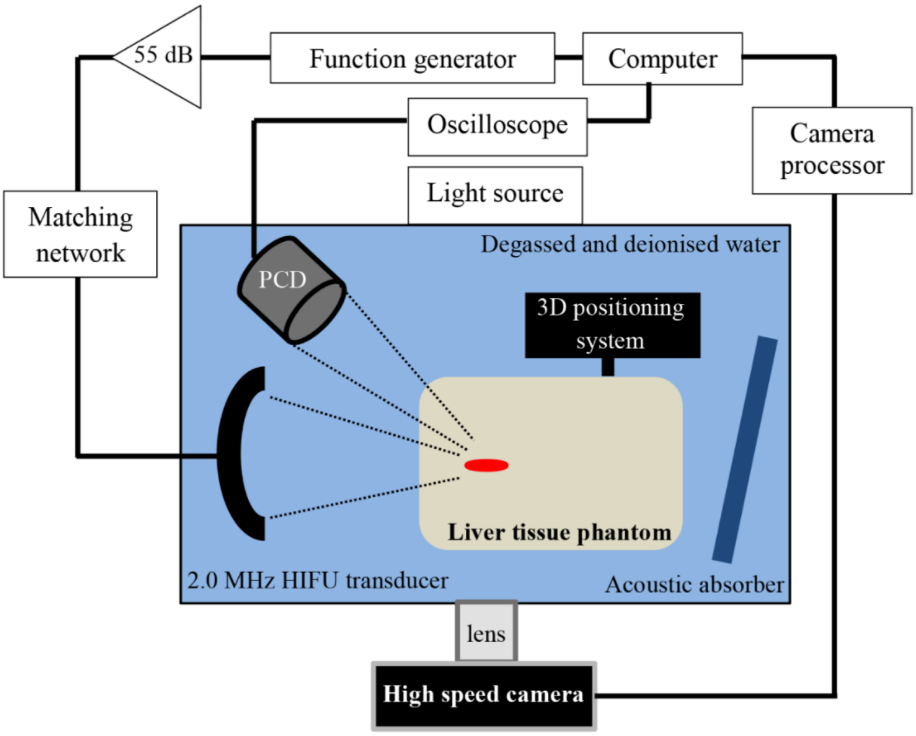

Fig. 2. A schematic diagram of the HIFU experimental setup used.

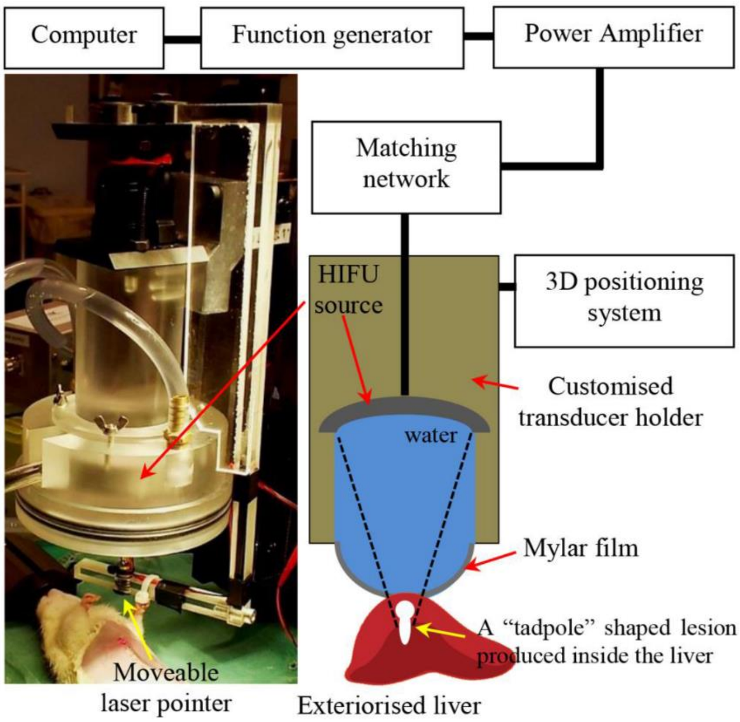

Fig. 3. A schematic diagram of the *in vivo* experimental setup used.

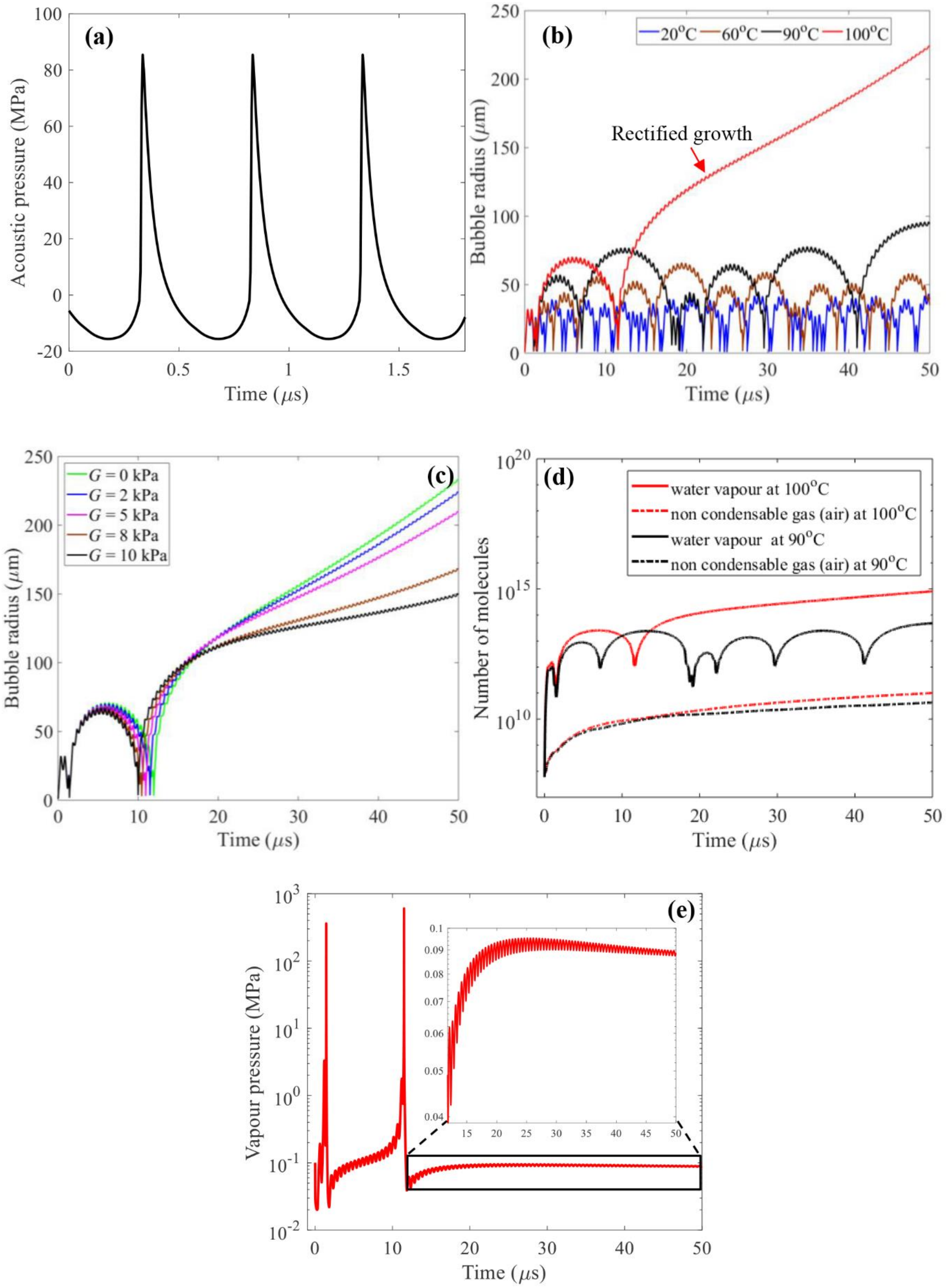

Fig. 4. Simulated single bubble dynamics under a 2.0 MHz nonlinear-shocked wave in the liver over 100 acoustic cycles. (a) Nonlinear shocked-waves obtained by numerically solving the KZK equation used to excite a single bubble. (b) Radius vs time curve with varying T_0 (20, 60, 90, 100°C) at G = 2 kPa. (c) Radius vs time curve with varying shear modulus G (0, 2, 5, 8 and 10 kPa) at T_0 = 100°C. (d) Molecular contents (water vapour and air) vs time

curve at T_0 = 100°C and 90°C, G = 2 kPa. (e) Vapour pressure inside the bubble at T_0 = 100°C and G = 2 kPa. The initial bubble radii R_0 and the tissue relaxation time λ_{relax} were 1 μm and 3 ns [25] respectively.

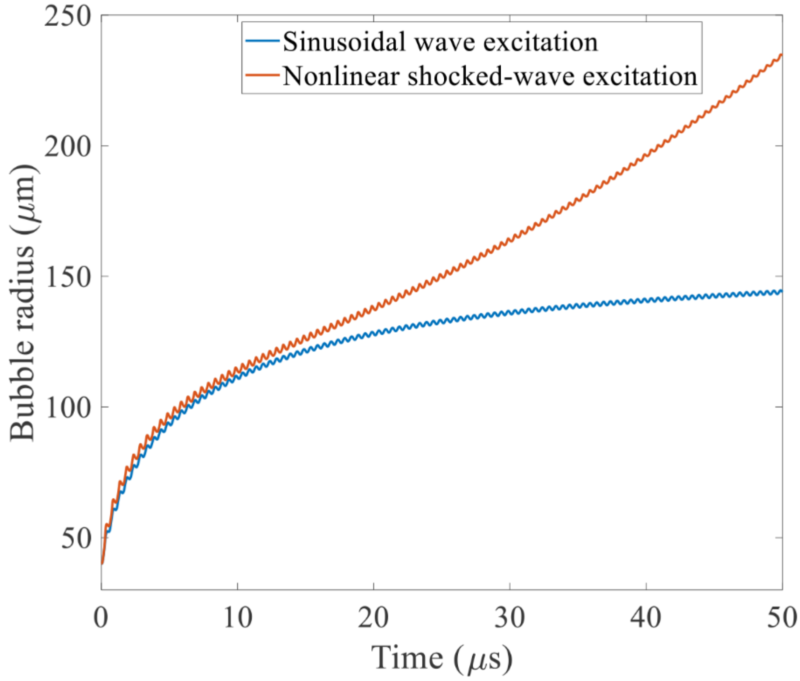

Fig 5. A comparison of the bubble dynamics in the liver (G = 2 kPa) under 2.0 MHz sinusoidal (P_- = – 15.6 MPa) and nonlinear-shocked (P_+ = 85.4 MPa; P_- = –15.6 MPa) excitations at T_0 = 100°C over 100 acoustic cycles. In the simulation, the initial bubble radius was chosen as R_0 = 40 μm as this clearly demonstrated the effect of the different shapes of the acoustic pressure waveforms on the bubble growth at 100°C without bubble collapses.

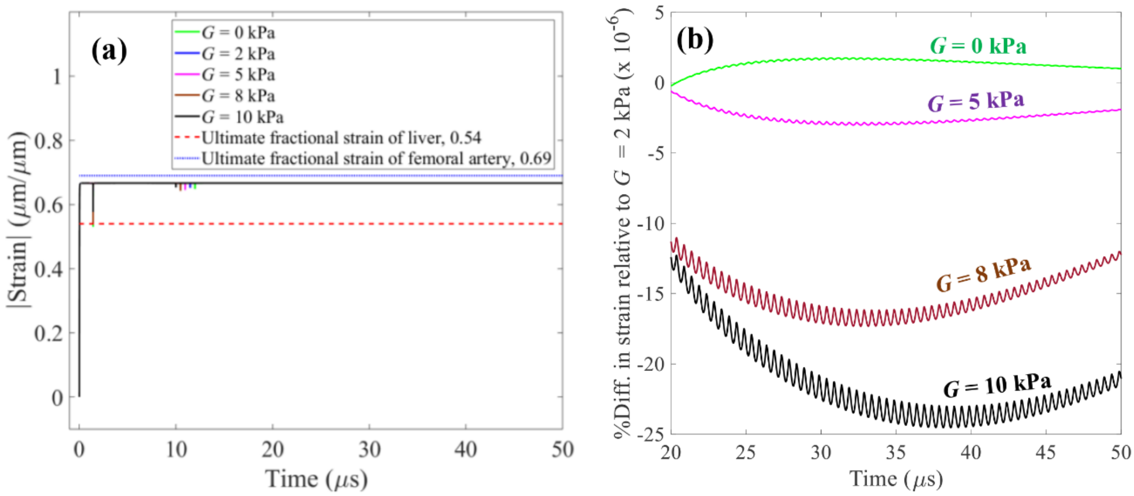

Fig. 6. Calculated a time-varying strain produced in the liver caused by rectified bubble growth at 100°C with varying shear modulus G. (a) Corresponding strain vs time curve of Fig. 4(c) over 100 acoustic cycles. (b) A percentage difference in strain (G = 0, 5, 8, 10 kPa)

relative to strain calculated at $G = 2$ kPa. The ultimate fractional strain values of liver tissue (0.54) and of femoral artery (0.69) ex vivo were obtained from [68].

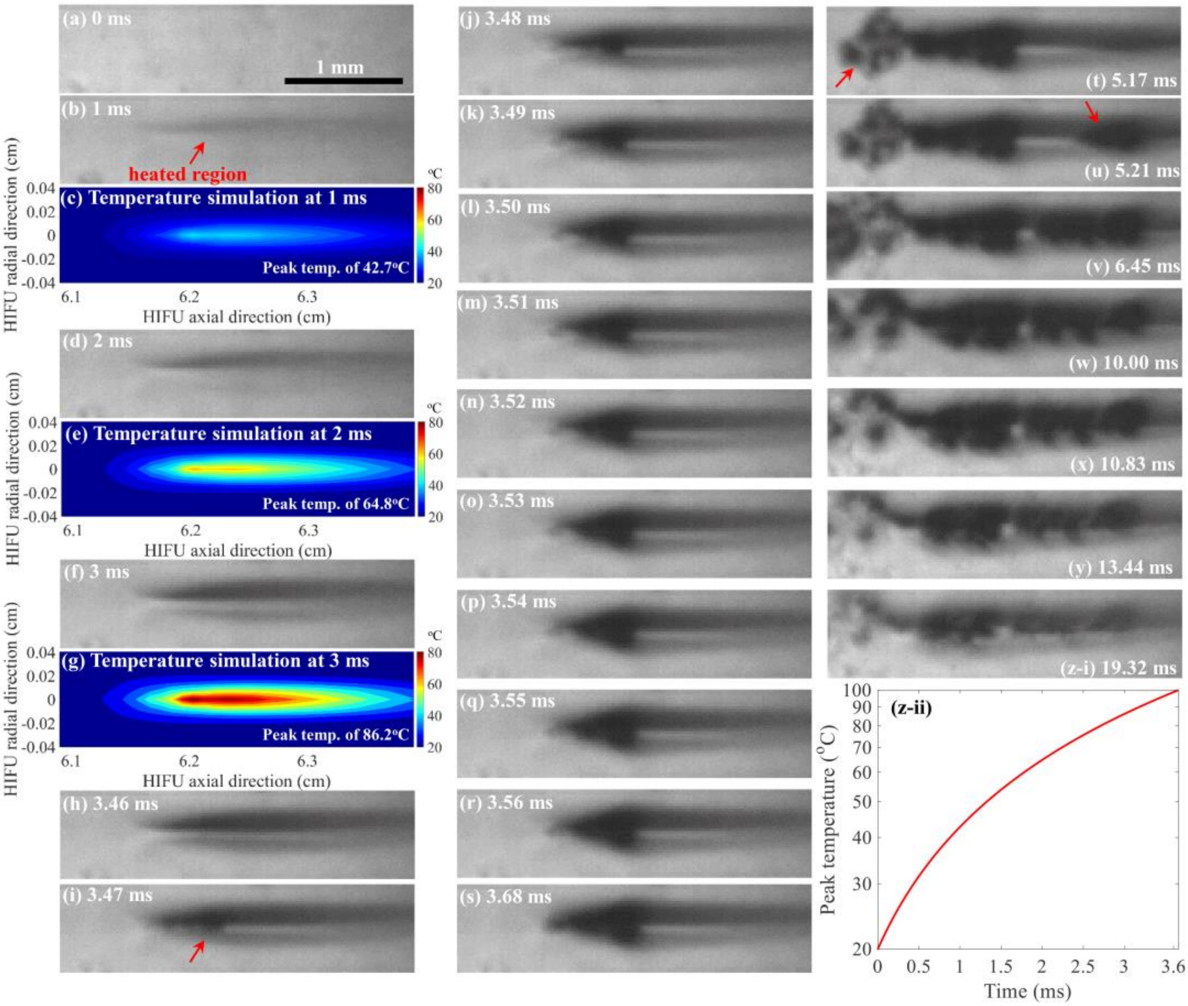

Fig. 7. A sequence of high-speed camera images obtained in an optically transparent liver tissue mimicking gel phantom during the single 10-ms HIFU exposure with P_+ of 85.4 MPa and P_- of –15.6 MPa. These images were filmed at a 100,000 fps. The 2.0 MHz HIFU beam propagates from left to right. The times at 0 ms (a) and 10 ms (w) correspond to the start and the end of the HIFU exposure respectively. (c), (e) and (g) represent simulated temperature contour plots at t = 1, 2 and 3 ms respectively. Images (x, y, z-i) were captured 0.83, 3.44 and 9.32 ms after the HIFU ceased at 10 ms. (z-ii) Computed peak temperature at the HIFU focus in the tissue phantom.

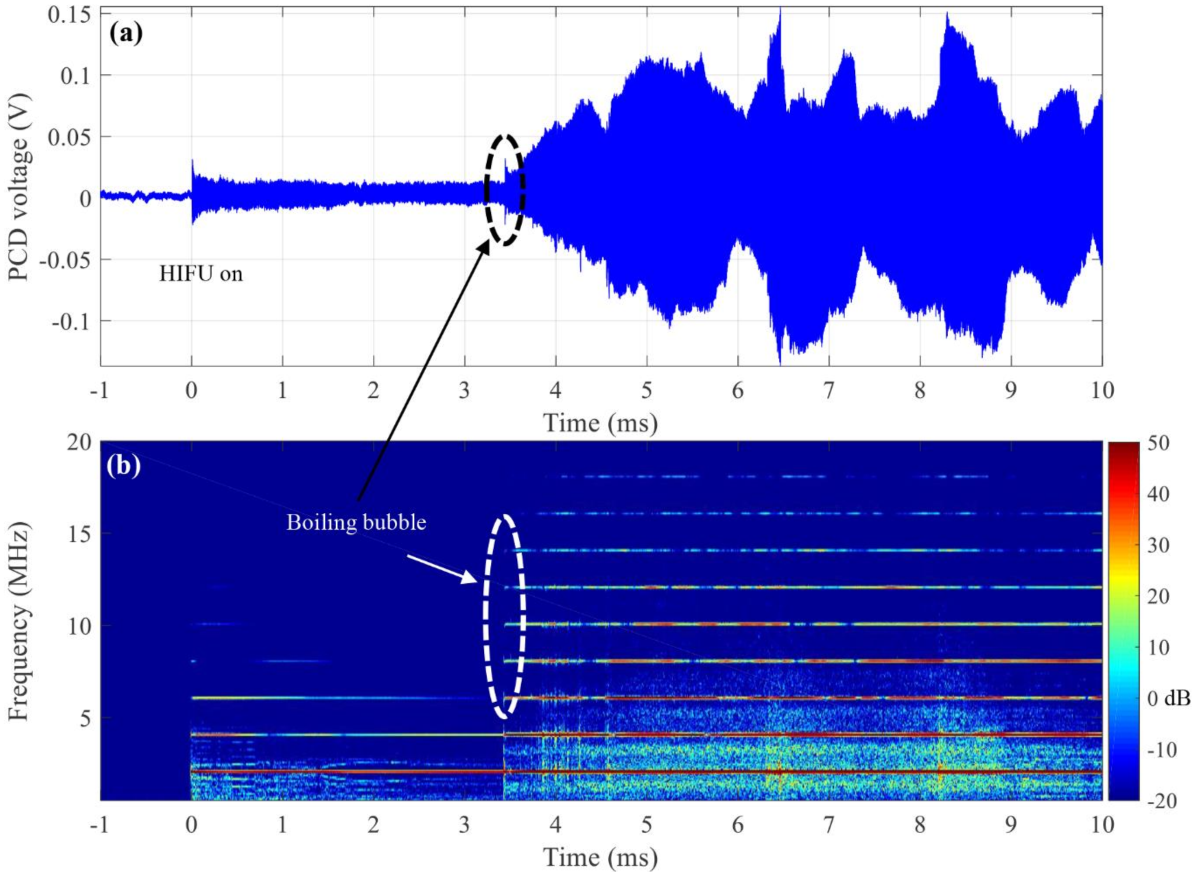

Fig. 8. Acoustic signal emitted from the HIFU focus in the gel phantom during the single 10-ms HIFU pulse. (a) The PCD voltage versus time plot and (b) the corresponding spectrogram. Acoustic emissions were recorded at a sampling frequency of 0.5 GHz. The time at 0 ms represents the start of the HIFU exposure.

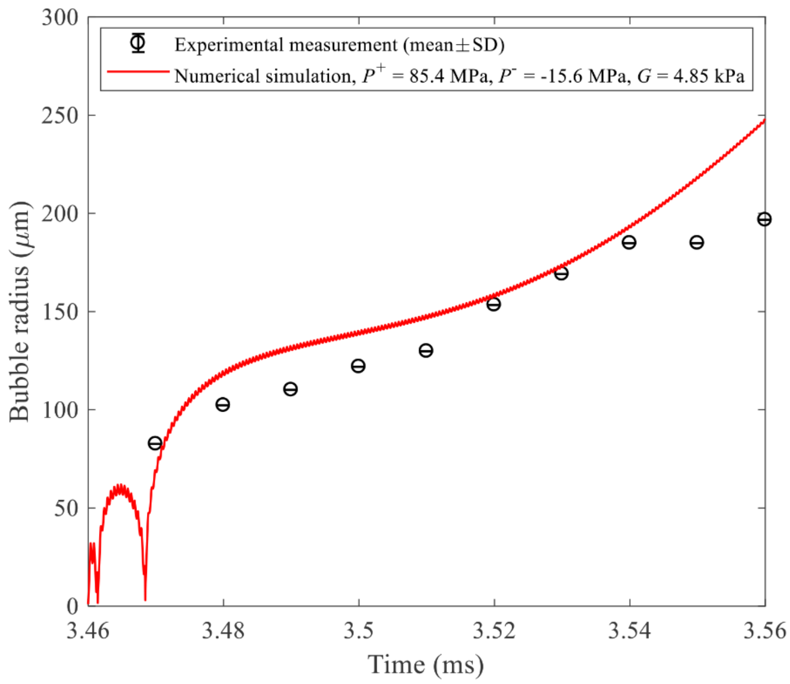

Fig. 9. A comparison between the experimentally measured bubble radius (mean ± standard deviation SD) and the simulated radius vs time curves. The simulation was performed at the

temperature of T_0 = 95.62°C which was obtained from the BHT simulation at t = 3.47 ms. Physical properties of the tissue phantom were obtained using Eqs. (33)–(37) at T_0 = 95.62°C. Shear modulus of G = 4.85 kPa of the liver tissue phantom [69] used in the present study was included in the simulation with R_0 = 1 µm. Photron FASTCAM Viewer software (Photron, San Diego, CA, USA) was employed for the size measurement (24 µm/pixel). Each measurement was repeated three times. A movie showing the presence of rectified bubble growth starting from at t = 3.47 ms is available in supplementary 1.

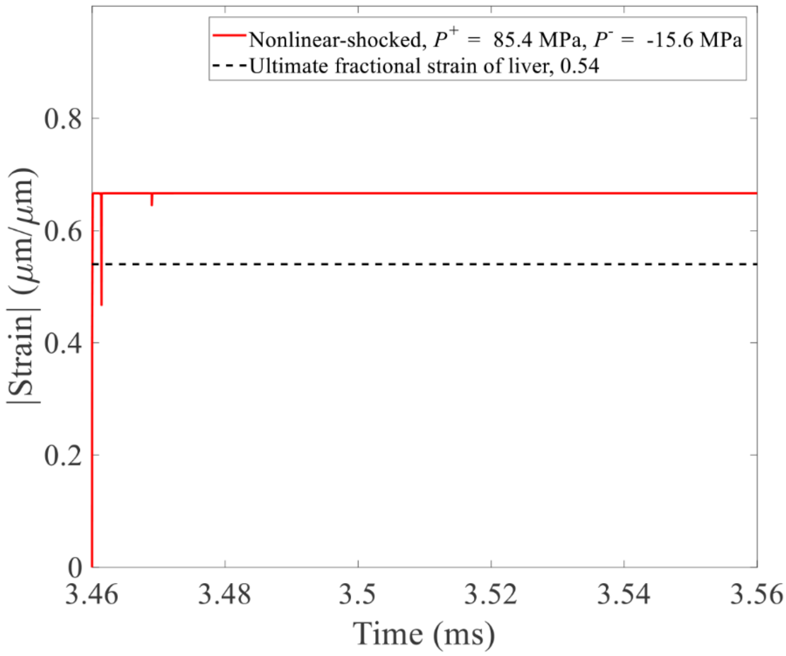

Fig. 10. Corresponding computed strain curve of Fig. 9 at G = 4.85 kPa. The ultimate fractional strain of the tissue phantom was assumed to be equal to that of the porcine *ex vivo* liver tissue of 0.54 [68].

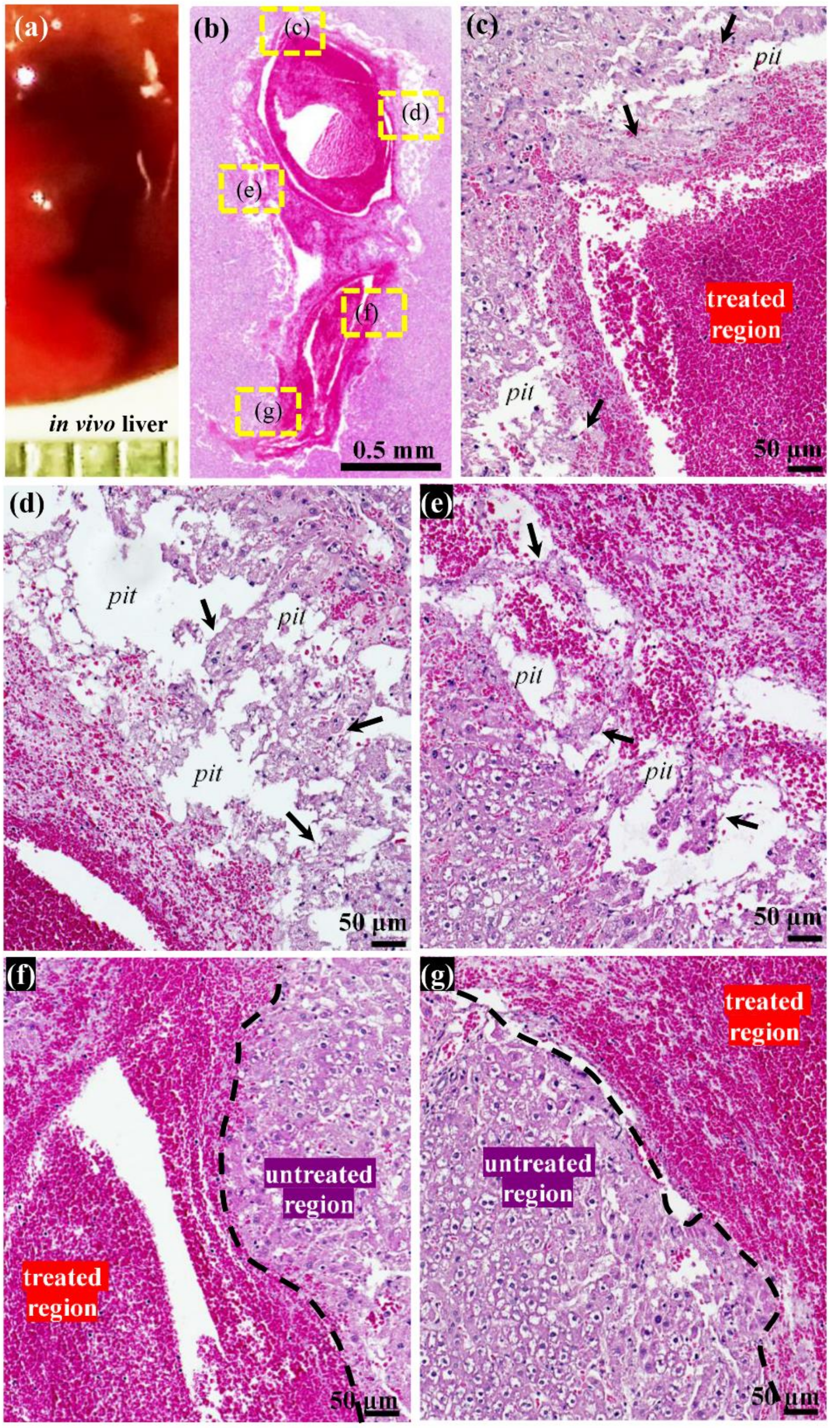

Fig. 11. Histological examination around a freshly created cavity produced by an electrical power of 200 W (simulated *in situ* P_+ = 80 MPa, P_- = –15.6 MPa) with 1% duty cycle, 1 Hz PRF and 10 HIFU pulses. (a) A photograph showing the cavity creation *in vivo*. The 2.0 MHz HIFU beam propagates from top to bottom. (b) Corresponding H&E stained lesion. Images (c) to (f) show the highlighted areas in (b) at higher magnifications. Arrows indicate broken hepatocyte plates.

Tables

Table 1. The alphabetical constants in Henry's law and the diffusion volumes for N_2, O_2 and Ar.

Gases	A_h	B_h	C_h	V_m [49]
N_2 [47]	–67.4	86.3	24.8	18.5
O_2 [48]	–66.7	87.5	24.5	16.3
Ar [49]	–57.7	74.8	20.1	16.2

Table 2. The number of translational and rotational degrees of freedom f_i, the characteristic vibrational temperatures θ_n and the number of the characteristic vibrational temperatures n for N_2, O_2, Ar and H_2O [43].

Gases	f_i	θ_n	*n*
N_2	5	3350	1
O_2	5	2273	1
Ar	3	-	-
H_2O	6	2295, 5255, 5400	3

Table 3. Physical constants for the gas dynamics used in the bubble model [41, 50].

Symbol	Definition	Value	Units
R_{gas}	Universal gas constant	8.314472	J mol^{-1} K^{-1}
K_B	Boltzmann constant	$1.3806503 \times 10^{-23}$	J K^{-1}
N_A	Avogadro's constant	$6.02214179 \times 10^{23}$	mol^{-1}
M_{air}	Molar mass of air	28.97×10^{-3}	kg mol^{-1}
M_{vap}	Molar mass of water vapour	18.015268×10^{-3}	kg mol^{-1}
M_{N2}	Molar mass of nitrogen	28×10^{-3}	kg mol^{-1}
M_{O2}	Molar mass of oxygen	31.9988×10^{-3}	kg mol^{-1}
M_{Ar}	Molar mass of argon	39.95×10^{-3}	kg mol^{-1}

Table 4. Physical properties of water and of liver measured at 20°C. These values were from [55, 56, 61].

		Values measured at 20°C		
Symbol	**Definition**	**Water**	**Liver**	**Ratio**
ρ_0	density [kg m^{-3}]	998.2	1060	1.06
c_0	speed of sound [m s^{-1}]	1482	1575	1.06
μ_0	viscosity [kg m^{-1} s^{-1}]	1.0019×10^{-3}	9×10^{-3}	8.98
σ_0	surface tension [N m^{-1}]	0.073	0.056	0.77

Table 5. Composition of 50 mL gel with 7% concentration of BSA. BSA = bovine serum albumen. TRIS = tromethamine. APS = ammonium persulfate. TEMED = tetramethylethylenediamine.

Components	Quantity	Percent (%)
Degassed and de-ionised water	35.805 mL	71.61
BSA	3.5 g	7
1 M TRIS	5 mL	10
40% Acrylamide	8.75 mL	17.5
10% APS	0.42 mL	0.84
TEMED	0.025 mL	0.05

Table 6. Physical properties of the liver *in vivo* used in the KZK and the BHT computations. These values were obtained from [64, 65].

Parameters	Values
small-signal speed of sound	1575 ms^{-1}
mass density	1060 kgm^{-3}
absorption at 1 MHz	52 dBm^{-1}
exponent of absorption vs frequency curve	1.1
coefficient of nonlinearity	4.4
specific heat capacity	3628 $Jkg^{-1}K^{-1}$
perfusion rate	19.5 $kgm^{-3}s^{-1}$
ambient temperature	37°C

Table 7. Physical properties of the liver used in the present bubble model. These values were obtained using Eqs. (33) – (37).

	Definition	Liver properties at T_0			
		T_0 = 20°C	60°C	90°C	100°C
ρ_L	density [kg m^{-3}]	1058	1042	1023	1015
c_0	speed of sound [m s^{-1}]	1575	1648	1647	1640
μ_0	viscosity [kg m^{-1} s^{-1}]	0.0087	0.004	0.0026	0.0023
σ_0	surface tension [N m^{-1}]	0.056	0.051	0.047	0.045
P_0	ambient pressure [Pa]	1.01325×10^5			
M	empirical material dependent constant	5.527 [9]			
A	empirical material dependent constant	614.6 [MPa]			
B	empirical material dependent constant	$A - p_0$ [MPa]			

Table 8. Characteristic timescales of gas diffusion and of bubble dynamics over 100 acoustic cycles. The diffusion coefficients at T_0 = 100°C were obtained from [39]. Corresponding bubble radius vs time curve at 100°C is plotted in Figure 4(b).

	Equations used [76]	Diffusion coefficients D at T_0 = 100 °C (m^2/s) [39]	Characteristic timescales (s)
O_2 diffusion		1.0336×10^{-9}	19.39
N_2 diffusion	$\tau_{gas} = \mathrm{mean}(R^2/D)$	9.58×10^{-10}	20.92
Ar diffusion		1.0374×10^{-9}	19.31
Bubble period	$\tau_{bubble} = \mathrm{mean}(R/\lvert\dot{R}\rvert)$	-	1.01×10^{-4}

Supplementary file

Supplementary 1. The movie shows the appearance of rectified bubble growth at the HIFU focus in the optically transparent tissue phantom during the course of boiling histotripsy exposure. A boiling vapour bubble forms at t = 3.47 ms.